Memoirs of the Faculty of Science, Kyoto University, Series of Physics, Astrophysics, Geophysics and Chemistry, Vol.XXXXIII, No.1, Article 1,2002

Coherent time evolution of highly excited Rydberg states in pulsed electric field: opening a stringent way to selectively field-ionize the highly excited states

By

Masaru Tada

Nuclear Science Division, Institute for Chemical Research, Kyoto University
Gokasho, Uji, Kyoto 611-0011, Japan

(*December 11, 2000)*

Abstract

We have investigated the properties of highly excited Rydberg states to establish a way to detect highly excited states selectively with pulsed field ionization method and to see possible coherent effects in highly excited Rydberg states with $n > 90$ in pulsed electric field. The experiment on the field ionization process of the Rydberg states with the principal quantum number $n = 98 - 150$ in ^{85}Rb has been carried out. For the first time, it has been observed that the electric field necessary to ionize the Rydberg states takes discrete values successively depending on the slew rate. Specifically the slew-rate dependence of the ionization field has varied with the quantum defect value of the states, *i.e.*, with the energy position of the states relative to the adjacent manifold. This transitional behavior in the field ionization shows regular dependence on the principal quantum number n, thus indicating that this behavior is quite general and applicable to a wide range of higher-lying Rydberg states. From these characteristic behaviors, it is strongly suggested that the coherence in the time evolution under the pulsed electric field plays decisive role in field ionization. By selecting the shape of the pulse of the applied electric field properly, it is therefore possible to stringently select a low-ℓ state from the close-lying states by field ionization. The differences in the field ionization values have been found to be large enough, for example, the field ionization value for $111s$ state has been as three times as

that for the $111p$ state. The transitional behavior observed here brings us a new powerful method to selectively field-ionize the low ℓ states from the many close-lying states, thus opening a new way to apply the highly excited Rydberg states to fundamental physics research.

Contents

1 Introduction

Highly excited Rydberg states [1] have many interesting properties and provide ideal and versatile situations in various field of physics. Particularly, since the Rydberg atoms are coupled strongly to electromagnetic field, they play important roles in the field of the cavity quantum electrodynamics (cavity QED) [2]. For example, Hullet *et al.* carried out an experiment to suppress spontaneous emission in the circular orbit Rydberg state in cesium [3]. By suppressing spontaneous emission, it becomes possible to reduce the natural width in spectroscopic experiments and to improve the significance in measurements of many physical constants. In another example of experiment, Meschede *et al.* realized a single atom maser in a superconducting cavity [4]. Using single atom maser, it was possible to determine the statistics for a small number of photons in a cavity [5]. Also Rydberg states have been suggested to be utilized for the quantum computation [6]. As an example of such development, Rauschenbeutel *et al.* realized a quantum phase gate operating on quantum bits carried by a single Rydberg atom and a zero- or one-photon field in a high-Q cavity. This gate is an essential tool for nondestructive measurement of single photon and for manipulation of many-qubit entanglement in cavity QED.

Although Rydberg atoms have great potentiality for taking an active part in the various field of physics as described above, the highly excited Rydberg states with principal quantum number n greater than 80 have not been well utilized so far. This situation is partly due to the lack of detailed knowledge on the properties of such highly excited Rydberg states, and also due to the increasing difficulty in the selective detection of a particular state among many close-lying states. The purposes of our present experiment are to investigate the properties of such highly excited Rydberg states and then to open a stringent way to selectively field-ionize the highly excited states for applying such states to studies of fundamental physics. In this thesis, the experimental results on the field ionization process of the Rydberg states with the principal quantum number n ranging from 98 to 150 in rubidium (^{85}Rb) under pulsed electric field are presented and discussed. As an introduction for this thesis, two concrete purposes in the present experiment are described as follows.

Rydberg atoms in the axion search experiment

In the astroparticle physics, it is one of the most important problems to clarify the character of the dark matter which occupies the most part of the matter energy in the Universe [7, 8]. According to the recent arguments in cosmology, it is the most promising model that the universe consists of 35 % of

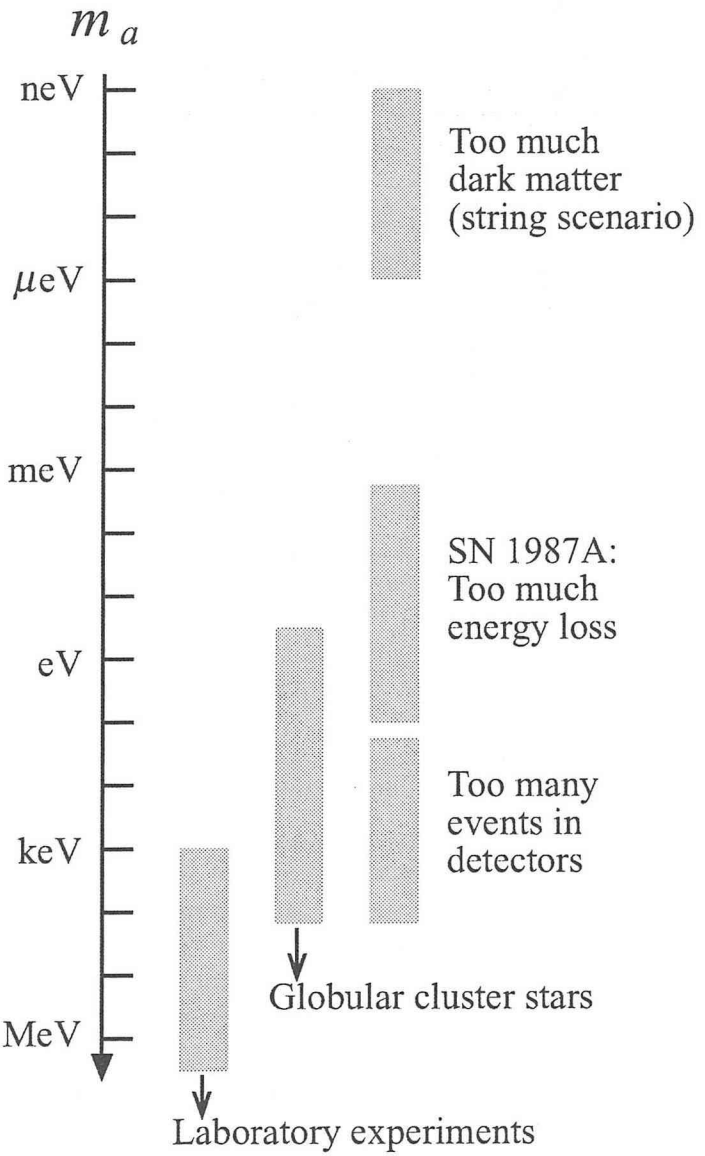

Figure 1: Summary of astrophysical and cosmological bounds to axion mass [11].

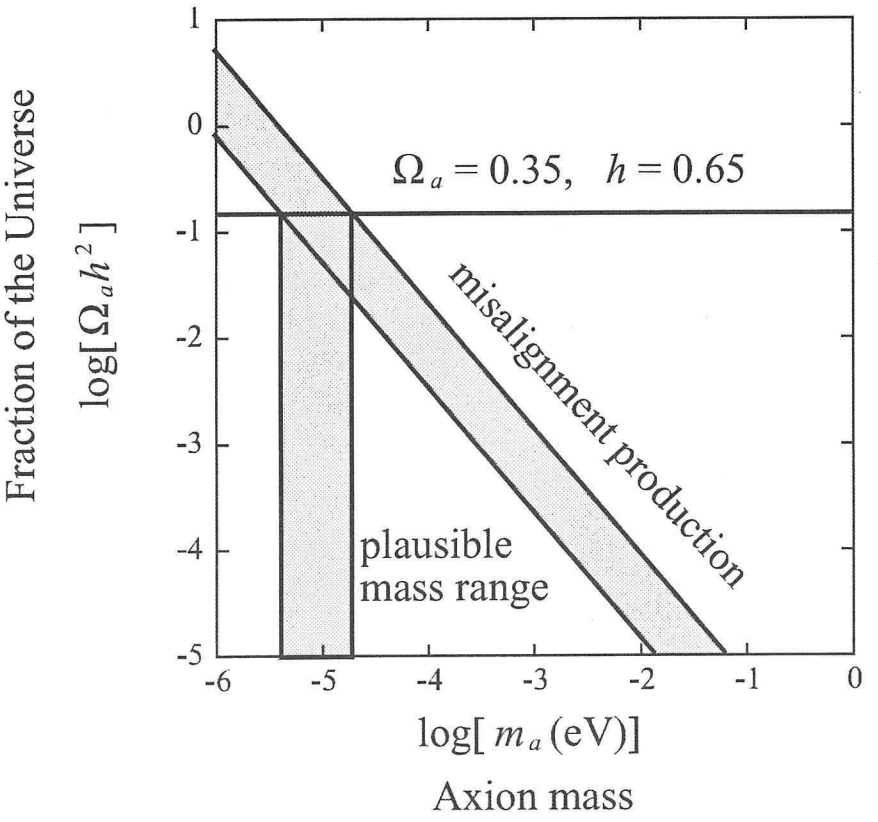

Figure 2: The most promising axion mass from the misalignment production.

the cold dark matter and 65 % of the dark energy (or cosmological constant) [9]. The axion, which was invoked in the quantum chromodynamics (QCD) to solve the strong CP problem [10], is one of the most promising candidates for the non-baryonic cold dark matter particles in the Universe. The mass (m_a) window of axions still open is between 1 μeV and 1 meV (Fig. 1). According to Raffelt's analysis [12], a plausible mass range for dark matter axions lies from 6 μeV to 250 μeV or 2 meV. Furthermore if the whole part of cold dark matter consists of the axions and the axions were created from the misalignment production in the early Universe [13], the axion mass is predicted to be about 10 μeV as the cold dark matter occupies the 35 % fraction of the energy density in the Universe (see Fig. 2).

Although many ideas have been proposed to search for dark matter axions, it seems now the most efficient way for the dark matter axion search to utilize the Primakoff process [14]. Fig. 3 shows the schematic diagram

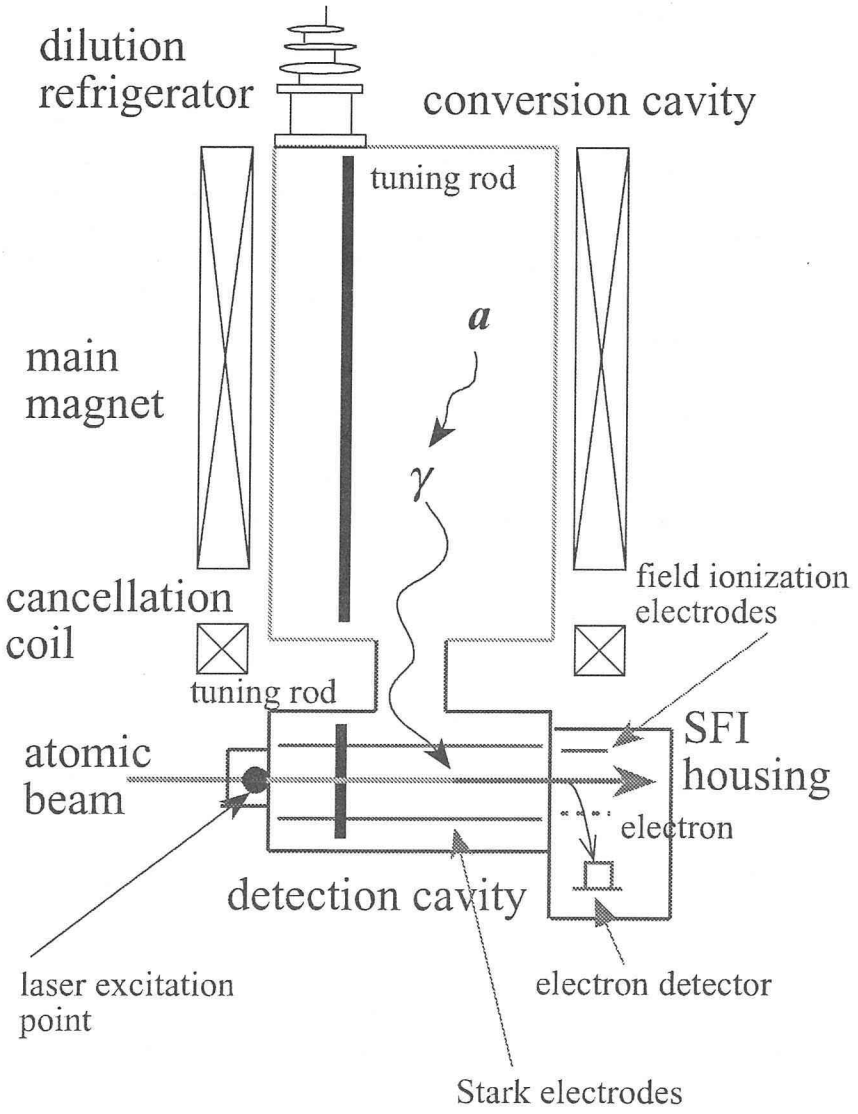

Figure 3: Schematic diagram of our experimental system called CARRACK to search for axions (cited from Ref.[18]).

of our experimental system called CARRACK (Cosmic Axion Reseach with Rydberg Atoms in resonant Cavities in Kyoto) to search for axions over a wide range of mass with the Primakoff process [15,16,17,18,19]. The principle of axion detection in CARRACK is as follows. The axion is converted into a photon in a cavity (conversion cavity) exposed to a strong magnetic field. The converted photon is led into another cavity (detection cavity) via a coupling hole. Atoms (^{85}Rb) in the ground state from an atomic beam source are excited to a Rydberg state by two-step laser excitation just in front of the detection cavity. Passing through the detection cavity, Rydberg atoms absorb the axion-converted-photons and are excited to the upper state. Transition frequency between the upper and the lower Rydberg states is set to be equal to the cavity resonant frequency. The Rydberg atoms in the upper state are selectively ionized by means of the field ionization. The electrons from the Rydberg states are detected by an electron detector. To reduce the thermal background photons in the cavity, the whole cavities and field ionization system are cooled down to 10 mK range with a dilution refrigerator.

The frequency of the converted photon lies in the microwave range. The characteristic feature of CARRACK is thus to use the Rydberg atom as a detector for the axion-converted photon. Although Rydberg atoms have various interesting characteristics, two of them are the most important for our experiment as seen later in section 2:

1) in the highly excited Rydberg states, the energy difference between n and $n+1$ levels lies in the microwave range.

2) the electric diploe transition probability between n and $n+1$ levels is very high due to the large overlap of the wavefunctions.

These indicate that the Rydberg atoms are very suitable for the microwave detector [20,21,22]. Quantum theoretical analyses [15,16,17,19] revealed that the Rydberg-atom single-photon detector in resonant cavities is very efficient for dark-matter-axion search.

In our system, most important things are how the noise from thermal blackbody photons is reduced and how the upper Rydberg state is detected separately from the lower Rydberg state. There have been, however, no experiments which investigated the characteristics of such higher excited Rydberg states with $n > 80$ in detail, partly because of the difficulty in selectively detecting a particular state from many close-lying states; in such highly excited states, the field ionization process generally occurs both through the non-adiabatic and adiabatic transitions, resulting multiple ionization threshold and the selective detection of a particular state becomes increasingly more difficult.

The first purpose of this experiment is thus to establish a way to detect such higher excited states selectively with the pulsed field ionization method.

Rydberg atoms in the coherent time evolution

Another interesting point is the effect of coherence in time evolution of state in pulsed electric field. Highly excited Rydberg states provide many ideal and versatile situation for investigating the coherence effects in the time evolution of a quantum system with many potential-energy curves that cross one another [23].

Before describing the coherent process, a simple model without effects of the coherent process is considered. As an example, in Fig. 4 (cited from Ref.[24]) shown is the calculated energy diagram of Rb $|m_j| = 1/2$ states in the electric field (called Stark map). Increasing the electric field, the energy levels shift and cross each other. On crossing points, they are traversed adiabatically or diabatically depending on the slew rate as to be described in detail in section 2.2. If the traversals are completely adiabatic in all the level crossing points, $18p$ state, for example, passes along the solid line. Such situation is called "purely adiabatic" in this thesis. In a similar way, if the traversals are completely diabatic, $18p$ state goes through the broken line ("purely diabatic"). But in fact, since each transition occurs with a certain probability depending on the slew rate in each crossing, the populated levels are distributed widely between the purely adiabatic and the purely diabatic paths. Further increasing the electric field, the levels reach the ionization thresholds finally and thus the ionization thresholds are also distributed widely.

In Fig. 5 (cited from Ref.[27]) shown is an example of experimental result for pulsed field ionization of Rydberg states in sodium. As the electric field reaches the field ionization threshold, continuously distributed levels are ionized, and thus the ionization signals are distributed widely between the purely adiabatic case and the purely diabatic case.

On the other hand, in the coherent process, the level crossings cannot be treated independently of one another and the transitions cannot be traced on the Stark map simply, since the interference among Stark levels cannot be ignored. Although the coherent effect is quite complicated and not easy to be interpreted strictly, it is predicted in Harmin's model calculation [23] with a simplified situation that only small number of levels are actually populated due to the interference effect and the ionization threshold has discrete values depending on the slew rate. Since the number of level crossings increases rapidly with increasing n, it is expected that the coherent effect plays more important role in higher excited Rydberg states than in lower excited states.

In the previous experiments for pulsed field ionization (sodium in [25,26,27,

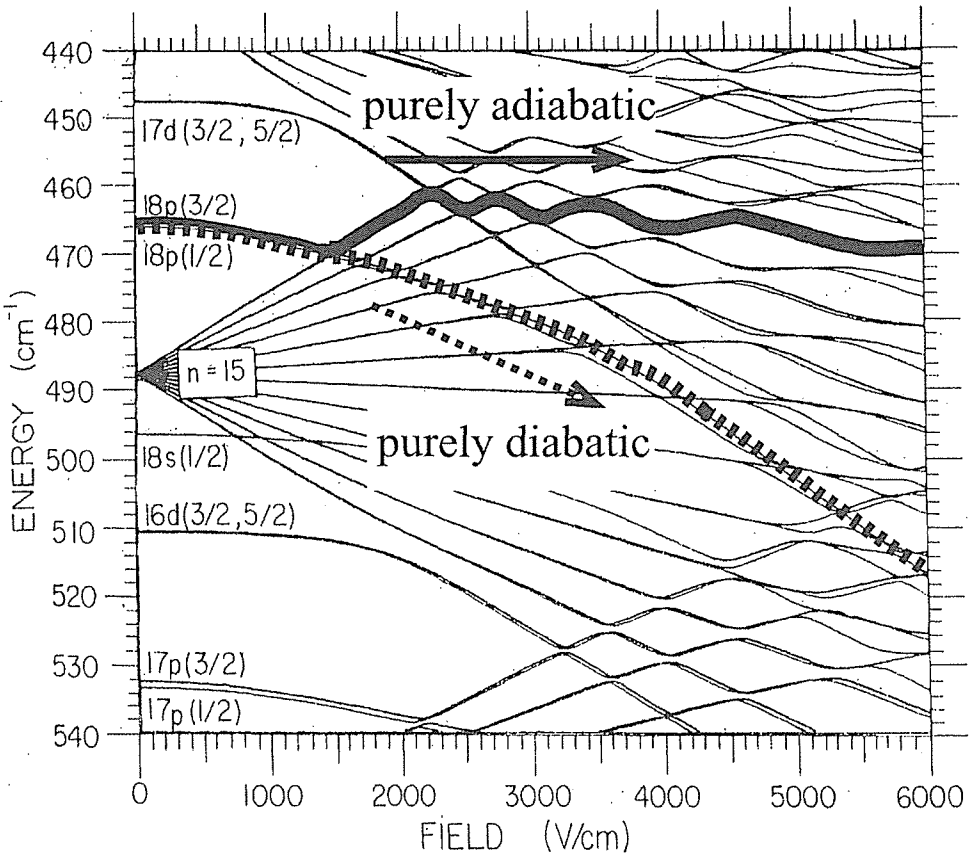

Figure 4: Calculated energy level diagram of Rb $|m_j| = 1/2$ states in a field (cited from Ref.[24]); in the "purely adiabatic" transition the level transits along the solid line, and in the "purely diabatic" transition along the broken line.

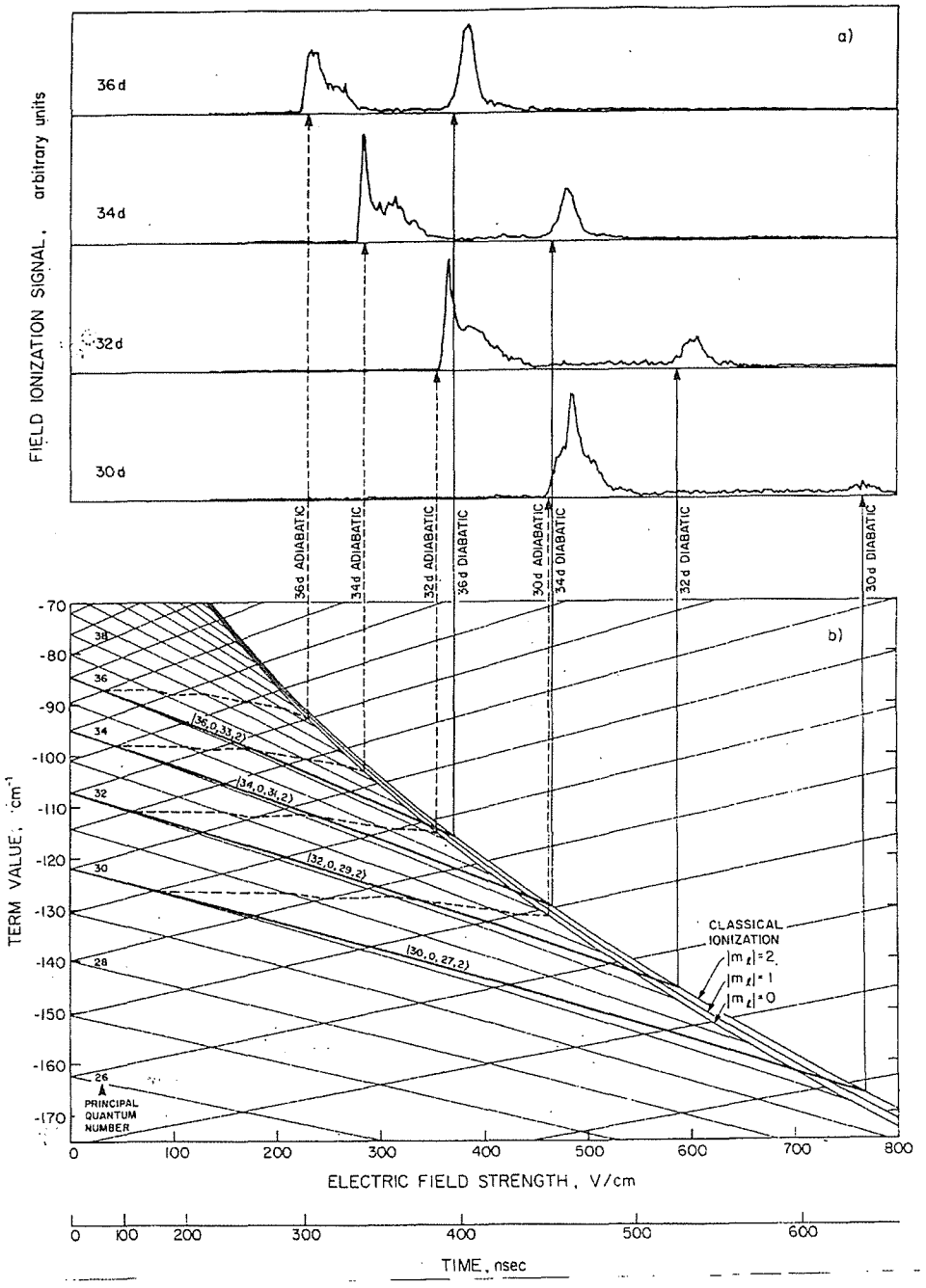

Figure 5: Field ionization data for Na nd states of $n = 30, 32, 34,$ and36 (cited from Ref.[27]). In the lower figure, solid lines show the purely diabatic paths and broken lines show the purely adiabatic paths.

28], potassium in [29], indium in [30]), Rydberg states for n up to 70 have been investigated and no detailed studies have been performed further for higher n states.

The second purpose of this experiment is thus to seek the possible coherent effect in highly excited Rydberg states as $n > 80$ in the pulsed electric field. Considering the previous results described above, we have investigated the behavior of Rydberg states with n ranging from 98 to 150 in the pulsed electric field.

As the result of the present investigation, the following points have been clarified. It has been observed for the first time that in high slew rate regime in the applied pulsed electric field, the field ionization process has a single threshold value: Specifically the ionization electric field has taken discrete values successively with increasing slew rate, and this dependence has varied with the position of the states relative to the adjacent manifold. This transitional behavior in the field ionization has shown regular dependence on the principal quantum number n, thus indicating that this behavior is quite general and applicable to a wide range of higher-lying Rydberg states. From these characteristic behaviors, it is strongly suggested that the coherence in the time evolution under the pulsed electric field plays decisive role in field ionization.

By selecting the shape of the pulse of the applied electric field properly, it is therefore possible to stringently select a low-ℓ state from the close-lying states by field ionization. The differences in the field ionization values were found to be large enough, for example, the field ionization value for $111s$ state is as three times as that for the $111p$ state.

In section 2, characteristics of a Rydberg atom and its behavior in the electric field are described in detail. In section 3, the experimental setup and procedures are described. The results of the present experiment are presented in section 4 and discussed in section 5. In section 5, the experimental results are especially discussed in the context of coherent and incoherent processes in the time evolution. The conclusion is in section 6.

2 Rydberg Atoms

2.1 General Characteristics of Rydberg Atoms

Rydberg atoms are highly excited atoms near to ionization limit with large principal quantum number n. Their binding energy is given by the Rydberg formula,

$$W_{n\ell} = R/(n-\delta_\ell)^2 = R/n^{*2}, \tag{1}$$

where R is the Rydberg constant 13.6 eV, δ_ℓ is the quantum defect of the states of angular momentum ℓ, and $n^* = n - \delta_\ell$ is the effective principal quantum number. For low ℓ states, the penetration and polarization of the ion core by the valence electron lead to large quantum defects and to strong departures from hydrogenic behavior. As ℓ increases, an orbit of valence electron becomes more circular and the atom becomes more hydrogenic. In particular for alkali atoms, the quantum defect of an $n\ell j$ state is given by

$$\delta_{n\ell j} = \delta_0 + \frac{\delta_2}{(n-\delta_0)^2} + \frac{\delta_4}{(n-\delta_0)^4} + \frac{\delta_6}{(n-\delta_0)^6} + \frac{\delta_8}{(n-\delta_0)^8}\cdots, \tag{2}$$

where δ_0, $\delta_2 \ldots$ are experimentally determined parameters for the alkali atoms. The parameters δ_0, $\delta_2 \ldots$ in Eq. 2 for ^{85}Rb are given in Table 1 (cited from Ref. [31]). Substituting Eq. 2 into Eq. 1, the binding energies of the levels, $W_{n\ell j}$ are given by

$$W_{n\ell j} = \frac{R_{\rm alk}}{(n-\delta_{n\ell j})^2}, \tag{3}$$

where $R_{\rm alk}$ is the Rydberg constant for the alkali atom.

The Rydberg atoms have following characteristics:

1) small energy difference between n and $n+1$ levels;
$\Delta W_n = W_{n+1} - W_n \approx R/n^{*3}$, $\Delta W_{100} \simeq 7$ GHz.

2) large $E1$ transition rate between n and $n+1$ levels;
$\langle n+1|\, er\, |n\rangle \propto n^{*2}$, $\Gamma_n\,(\sec^{-1}) \approx 10^5 n^{*4}\,(\Delta W_n\,(\mathrm{eV}))^3$,
$\Gamma_{100} \simeq 3\times 10^4\ \sec^{-1}$.

3) long life time;
$\tau_n \propto n^{*3}$ (for $\ell \ll n$), $\tau_{100} \approx 1$ msec. $\tau_n \propto n^{*5}$ (for $\ell \approx n$).

The above item 1) shows the energy difference between the adjacent Rydberg states lies in the microwave range. In the case of $n \sim 100$, for example, the wavelength of the microwave corresponding to the transition frequency

Table 1: ^{85}Rb quantum defect parameters [31].

Series	δ_0	δ_2	δ_4	δ_6	δ_8
$ns_{1/2}$	3.13109(2)	0.204(8)	-1.8		
$np_{1/2}$	2.65456(15)	0.388(60)	-7.904	116.437	-405.907
$np_{3/2}$	2.64145(20)	0.33(18)	-0.97495	14.6001	-44.7265
$np_{3/2,5/2}$	1.347157(80)	-0.59553(18)	-1.50517	-2.4206	19.736

between n and $n+1$ is of the order of centimeter. The item 2) shows the Rydberg atom is strongly coupled with electromagnetic field in the microwave range. From 3) the transitions to the nearby states are dominant for $\ell \approx n$, while for $\ell \ll n$ the transitions near to the ground state are dominant. In the finite temperature, the total life time τ_n^t is given by

$$\frac{1}{\tau_n^t} = \frac{1}{\tau_n} + \frac{1}{\tau_n^{bb}} \tag{4}$$

where τ_n^{bb} is the life time induced by the blackbody radiation and

$$\tau_n^{bb} \propto \frac{n^{*3}}{T} \tag{5}$$

where T is the temperature. As an example, $\tau_{100}^{bb} \sim 1.9$ msec at 77K and $\tau_{100} \sim 1.3$ msec, and then $\tau_{100}^t(77\text{K})$ is about 0.8 msec.

2.2 Rydberg Atoms in the Electric Field

As seen above, the binding energy of valence electron in Rydberg atom decreases rapidly with increasing quantum number n and is strongly affected by the external field. In this section the behavior of Rydberg atoms in electric field is considered. The equations in this section are expressed in atomic units which are defined so that all the relevant parameters for the ground state of hydrogen have magnitude one (Table 2 [1]).

Consider first a hydrogen atom with its nucleus at the origin in the presence of an external field F along the z-axis. The potential experienced by an electron is given by

$$V(r) = -\frac{1}{r} - Fz, \tag{6}$$

and has a saddle point at $z_{\max} = 1/\sqrt{F}$ (see Fig. 6). The potential at the saddle point is

$$V_{\max} = -2\sqrt{F}. \tag{7}$$

Table 2: Atomic unit [1].

Quantity	Atomic unit	Definition
Mass	Electron mass	9.1×10^{-28}g
Charge	Electron charge	1.6×10^{-19}C
Energy	Twice the ionization potential of hydrogen	27.2eV
Length	Radius of a_0, the first Bohr orbit	0.529Å
Velocity	Velocity of the first Bohr orbit	2.19×10^{8}cm/sec
Electric field	Field at the first Bohr orbit	5.14×10^{9}V/cm

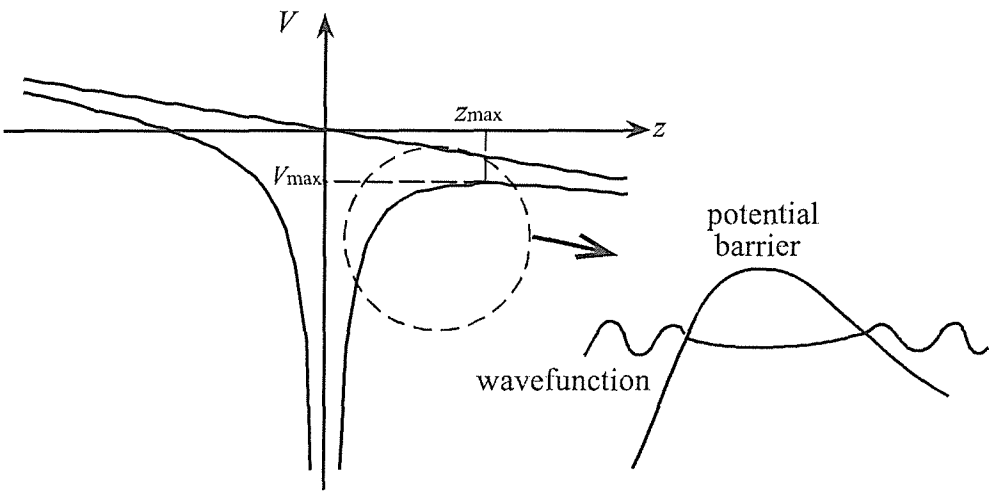

Figure 6: Combined Coulomb-Stark potential along the z axis with electric field in the z direction. A state can be ionized if its energy is enough for the electron to surmount the potential barrier.

Classically, the electrons with energy $W_n = -1/2n^2$ above $V_{\max}$ are ionized by the field. The classical threshold field for ionization of a state n is given by,

$$F_c = \frac{1}{16n^4} = 3.2\left(\frac{100}{n}\right)^4 \text{ V/cm.} \tag{8}$$

In an electric field the degeneracy of the energy levels is resolved in hydrogenic atoms and the levels split in proportion to the magnitude of the field (the first order Stark shift). The set of the energy levels degenerated in zero field for each principal quantum number n is called "manifold". The splitting due to electric field is given approximately as

$$\Delta W = \frac{3}{2}F(n_1 - n_2)n, \tag{9}$$

where n_1 and n_2 are the parabolic quantum numbers [1] and related to n and the magnetic quantum number m by

$$n = n_1 + n_2 + |m| + 1. \tag{10}$$

In Fig. 7 (cited from Ref. [32]) shown is the Strak structure of Hydrogen. The solid line shows the classical field ionization threshold described above and the broken line shows the first level crossing points given by

$$F_c = \frac{1}{3n^5} = 0.17\left(\frac{100}{n}\right)^5 \text{ V/cm.} \tag{11}$$

Although Eq. 8 is, in a practical sense, nearly exact also for non-hydrogenic atoms, the real ionization process is rather complicated. The field ionization for non-hydrogenic atoms is classified into two processes; adiabatic or diabatic. Consider the alkali atoms in a slowly rising field. In zero field, the energy of alkali atom is given by Eq. 3 in which the levels are ordered by the effective quantum number n^*. The zero field spacing between ℓ levels is given by $\Delta W = (\delta_\ell - \delta_{\ell+1})/n^3$.

In non-hydrogenic atoms the splitting begins from the second order Stark shift in the low ℓ states due to the presence of the finite-sized ionic core. The Stark shift ΔW of the low ℓ state $|nJm\rangle$ is given by

$$\Delta W = -\frac{1}{2}\alpha_0 F^2 - \frac{1}{2}\alpha_2 \frac{3m^2 - J(J+1)}{J(2J+1)}F^2, \tag{12}$$

where α_0 and α_2 are the scalar and tensor polarizabilities, respectively [1].

In Fig. 4 shown is the energy diagram of Rb $|m_j| = 1/2$ states in the electric field. It is noted that the degeneracy of low ℓ states, s, p and d, is

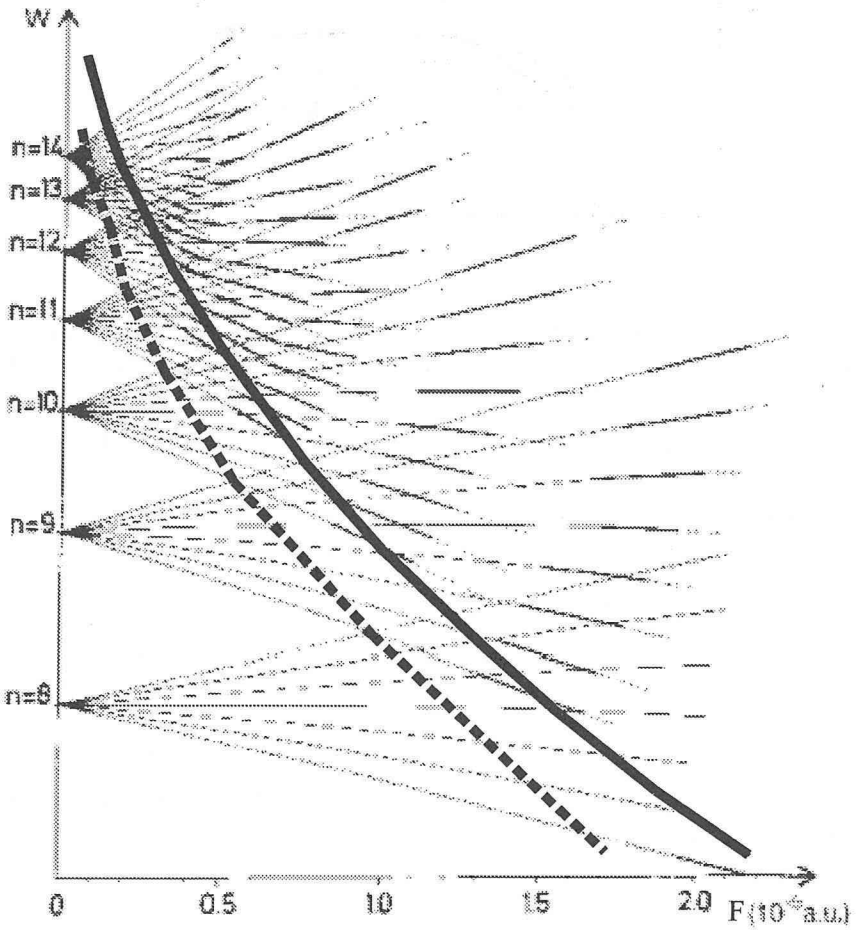

Figure 7: Strak structure of Hydrogen (cited from Ref.[32]). The solid line shows the classical field ionization threshold given by $F_c = 1/16n^4$ and the broken line shows the first level crossing points given by $F_c = 1/3n^5$.

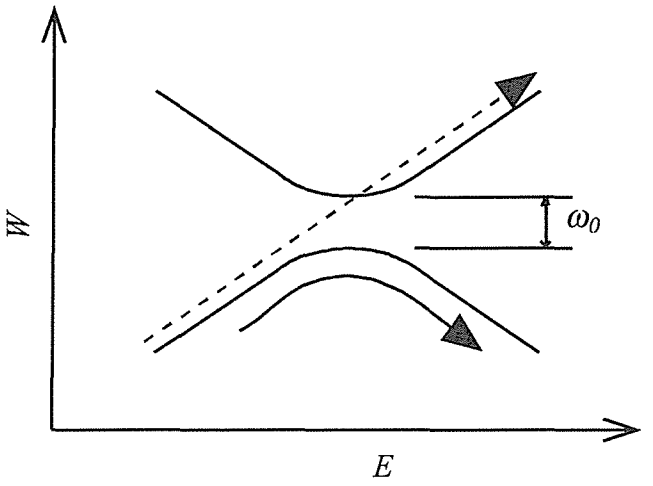

Figure 8: Two Stark levels with an avoided crossing of ω_0. An adiabatic passage is shown in solid arrow and a diabatic passage is in broken arrow.

resolved in zero field, and the p state locates above the manifold and the s and the d states below the manifold.

The second effect of the presence of the finite sized ionic core (*i.e.*, the presence of the nonzero quantum defects) is the avoided crossings between the Stark states. In zero field or low fields, ℓ is a good quantum number. When the field reaches a value such that the separation between Stark states, $3nF$, is equal to the above ΔW, the ℓ states are no longer good eigenstates. If the field reaches this value in comparable to or longer time than the inverse of ΔW, the passage is adiabatic.

When the field reaches $1/3n^5$, an avoided crossing with Stark states of the same m but adjacent n are encountered. Consider the isolated avoided crossing with the separation energy ω_0 between two levels (see Fig. 8). If the crossing is traversed slowly compared to $1/\omega_0$, the inverse of the magnitude of the crossing, the traversal is adiabatic (solid arrow in Fig. 8) and the atom remains in the same adiabatic energy level. If the crossing is traversed fast, the traversal is diabatic (broken arrow). The time differential of the electric field, slew rate, is defined as $S = dF/dt$. Defining S_x by

$$S_x = \frac{\omega_0^2}{\left(\frac{dW_1}{dF} - \frac{dW_2}{dF}\right)}, \tag{13}$$

where dW_1/dF and dW_2/dF are the Stark shifts for each levels, the adiabatic transition at the avoided crossing occurs by the probability D given by the

Landau-Zener formula [33],

$$D = \exp\left(-2\pi\frac{S_x}{S}\right). \tag{14}$$

In Fig. 4, if the traversals are completely adiabatic in all the level crossing points, $18p$ state passes along the solid line. The situation is called "purely adiabatic" in this thesis. In a similar way, if the traversals are completely diabatic in all the level crossing points, $18p$ state passes along the broken line ("purely diabatic"). In an actual situation it is generally the case that many levels are populated through many trajectories between the purely adiabatic and the purely diabatic paths, depending on the slew rate at each crossing.

2.3 Field Ionization

In Fig. 9 schematic diagram of the field ionization process on the Stark energy map together with the classical field ionization threshold line is shown. Upper half levels of the manifold are called "blue" states and the highest level is called the "bluest" state, while lower half levels called "red" states and the lowest level called the "reddest" state. In the Eq. 9 the bluest state corresponds to the case $n_1 - n_2 = n - 1$ and the reddest state $n_1 - n_2 = 1 - n$. In the case of purely diabatic, the bluest level passes along the trajectory (a) and the reddest level (d). The ionization thresholds of these states are given by

$$F_c(\text{bluest}) \sim \frac{1}{21n^4}, \tag{15}$$

$$F_c(\text{reddest}) \sim \frac{1}{9n^4}, \tag{16}$$

from Eq. 7 and 9. In the case of purely adiabatic, the bluest level and the reddest level pass along the trajectories (b) and (c) respectively, and then the ionization occurs when the field reaches $\sim 1/16n^4$.

In a hydrogenic atom, however, the ionization process does not behave in a similar way. In Fig. 10 shown is the energy levels of the Hydrogen $n = 15, m = 0$ Stark levels (cited from Ref. [1]). While the reddest state is ionized at the field $\sim 1/9n^4$, the bluest state is ionized at higher field. In Fig. 11 shown is an example of the charge distribution for hydrogen ($n = 8$) in electric field (cited from Ref. [34]) whose direction is shown with an arrow for each figure. The reddest state and the bluest state correspond to Fig. 11 (a) and (h), respectively. In the case of the reddest state, since the outer electron lies in the negative side in the direction of electric field, it is easy to ionize the electron. On the other hand in the case of the bluest state, since

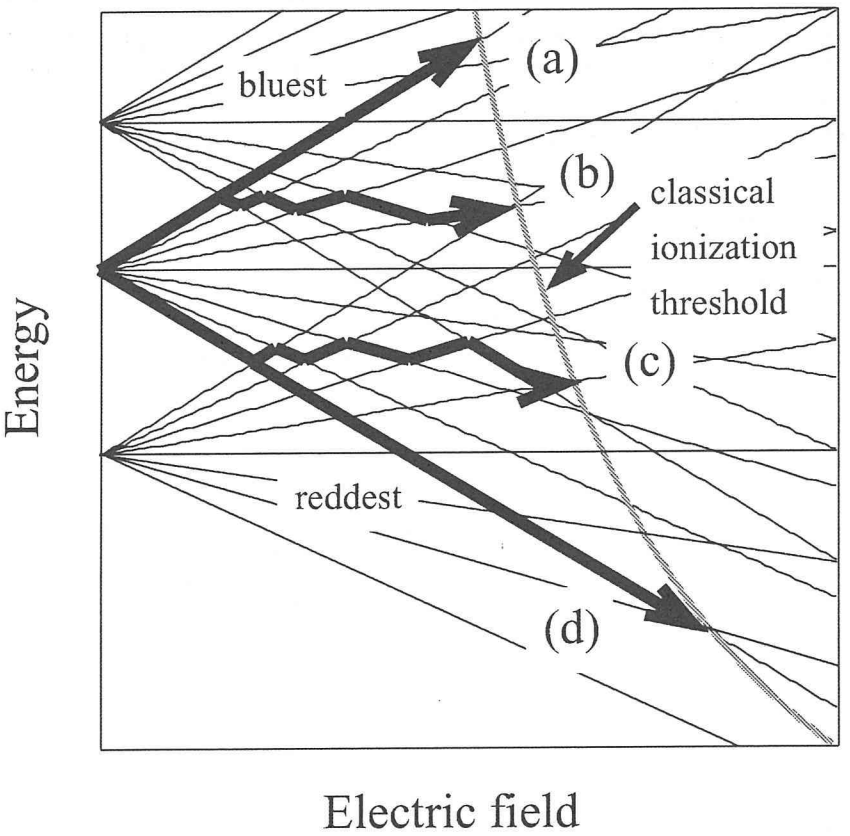

Figure 9: Schematic diagram of ionization process on the Stark energy map. The arrows (a) to (d) indicate possible trajectories for "purely adiabatic" ((b) and (c)) and "purely diabatic" ((a) and (d)) transitions.

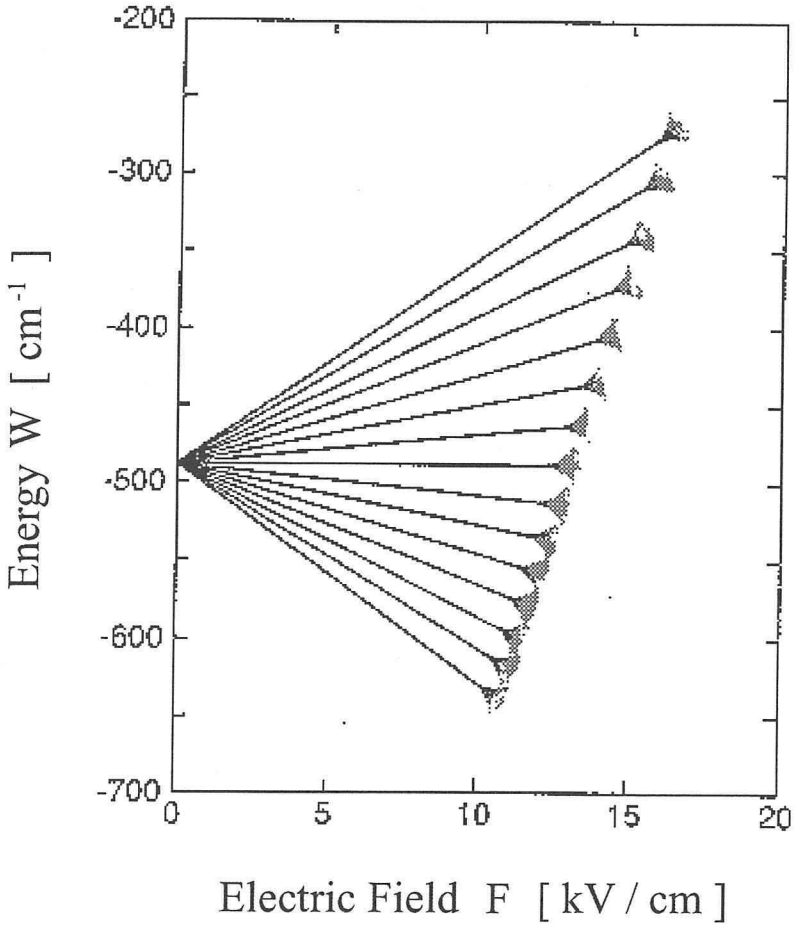

Figure 10: Energy levels of the Hydrogen $n = 15, m = 0$ Stark levels (cited from Ref.[1]).

the outer electron lies in the positive side in the direction of electric field, it is hard to ionize the electron.

In a non-hydrogenic atom, there are two forms of field ionization. The first is like hydrogen. A state of approximate quantum number n_1 can itself ionize, keeping the same value of n_1, in a field if its energy is enough for the electron to surmount the potential barrier (see Fig. 6). Rates for this form of ionization increase rapidly in the vicinity of the threshold for classical ionization, just as in hydrogen. In this form of ionization the blue states require higher fields for ionization than red states of the same energy. The second form of ionization is similar to autoionization [1]. In a non-hydrogenic atom n_1 is not a good quantum number and bound states of high n_1 are coupled to Stark continua of low n_1. Due to the influence of the crossing to the red states of the upper manifold, the ionization of the blue states occurs at lower electric field as described above (Eq. 15).

Since in practice the levels distribute continuously between the purely adiabatic way and the purely diabatic way depending on the slew rate in each crossing as mentioned above, the ionization threshold also distributes continuously depending on the slew rate. In Fig. 12 the variation of the field ionization signals with varying slew rate in the experiment of Neijzen *et al.* in indium atom is shown (cited from Ref.[30]). The trajectory ① shows the purely adiabatic path. In the trajectory ②, the level passes through adiabatically at the first crossing and diabatically at all the other crossings. In the trajectory ③, the levels pass through more diabatically. With increasing slew rate, at the first the component ② is increasing, and then the component ③ is more dominant, *i.e.*, the diabatic component is more dominant with increasing slew rate. It is noted that in the adiabatic path ① the ionization occurs as the non-hydrogenic type and in the diabatic path ②, ③ the ionizations occur as the hydrogenic type in this experiment.

As described above, it is, therefore, very important to control the slew rate for the selective field ionization. There are two ways to apply the electric field in the field ionization and they have different characteristics. In Fig. 13 two types of the time dependence of the applied electric field are shown. Fig. 13(a) shows the DC field in which the discrimination between different states comes from the adjustment of the strength of the field and only the geometry of the field ionization electrodes determines the slew rate. On the other hand, Fig. 13(b) shows the pulsed field in which the discrimination comes from the adjustment of the amplitude of the pulse and the slew rate can be controlled by adjustment of the rising time of the pulse. Since both the slew rate and ionization field can be controlled by adjustment of the shape of the pulse, the pulsed field ionization method is quite flexible and versatile.

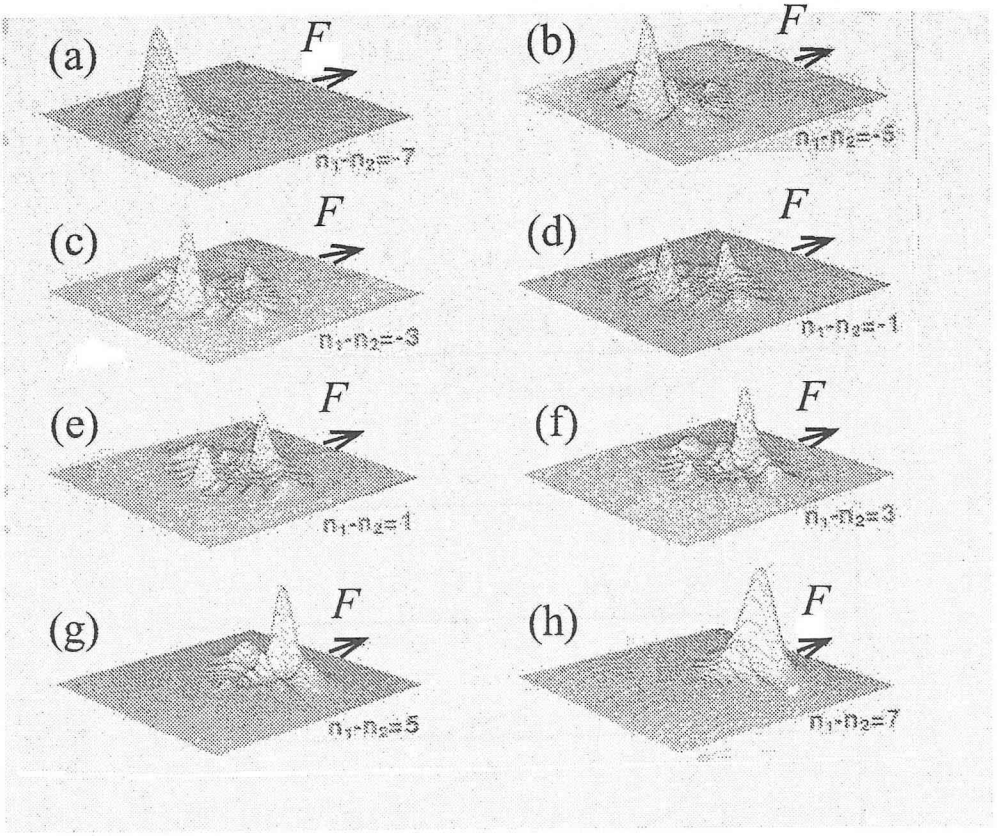

Figure 11: Charge distribution for hydrogen in electric field for "parabolic" eigenstates: $n = 8$, $m = 0$, $n_1 - n_2 = -7$ to 7 with the direction of electric field (cited from Ref.[34]). (a) and (h) show the reddest and the bluest states, respectively.

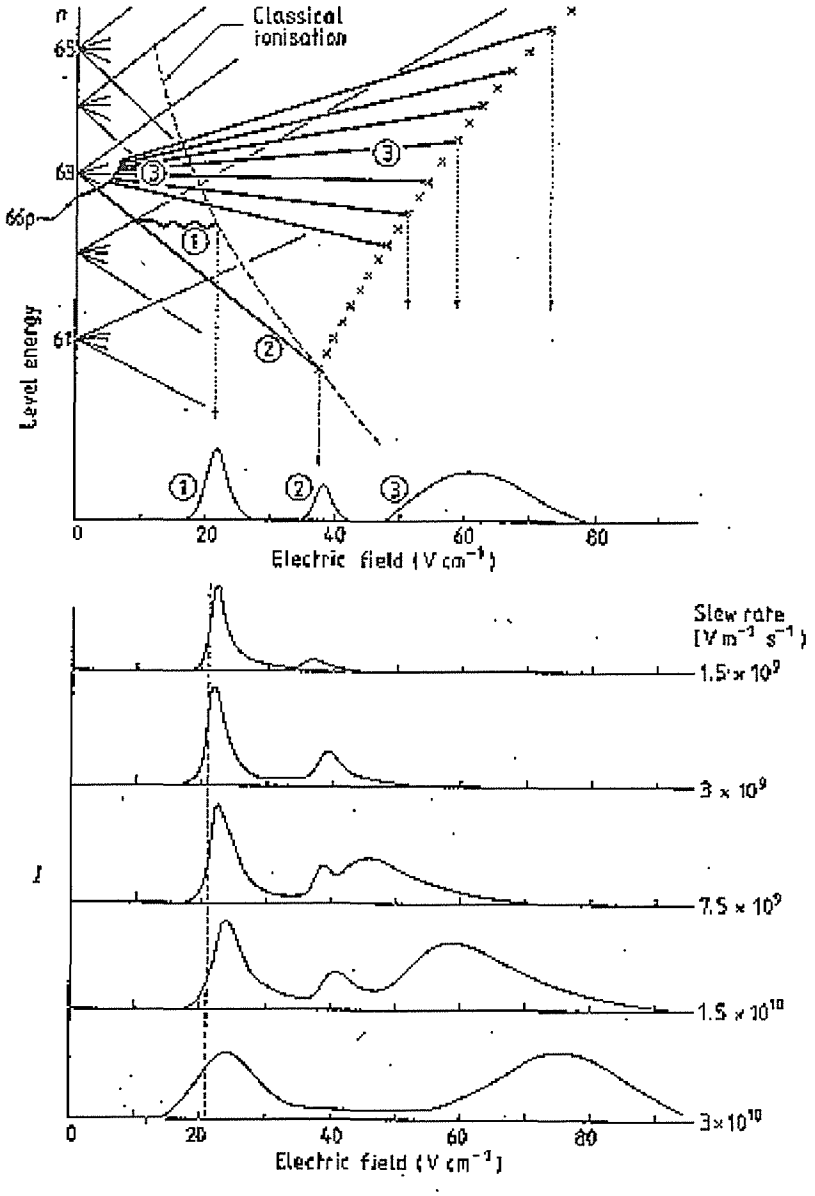

Figure 12: The ionization signal of $66p$ state of In as a function of the increasing electric field for various slew rates of the field pulse (cited from Ref.[30]). The upper part of the figure schematically explains the origin of the observed peaks. The diabatic component is more dominant with increasing slew rate.

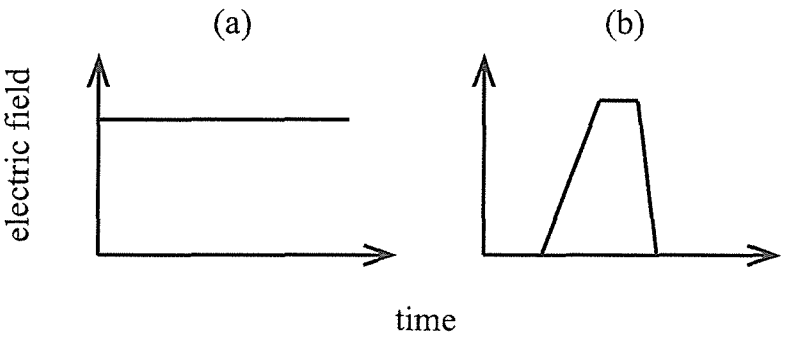

Figure 13: Shapes of applied electric field for the ionization region: (a) DC field; (b) pulsed field.

2.4 Production of Rydberg Atoms

Rydberg atoms can be produced by several ways. There are three methods for the production of Rydberg states often used.

1) electron impact

$$e^- + A \rightarrow A_{n\ell} + e^- \tag{17}$$

2) charge exchange

$$A^+ + B \rightarrow A_{n\ell} + B^+ \tag{18}$$

3) optical excitation

$$h\nu + A \rightarrow A_{n\ell} \tag{19}$$

If the $n \sim 100$ state of Rydberg atom is produced, the energy difference between adjacent levels corresponds to about 30 μ eV. Since the technology to make such a monochromatic electron beam has not been established, in the method of the electron impact nearly all energetically possible states are produced and then the excited Rydberg states have a certain distribution for the principal quantum number n. In the charge exchange method, it is not possible to produce the specified Rydberg level selectively, either. On the other hand, the optical excitation differs from collisional excitation in a fundamental way; the exciting photon is absorbed by the target atom. As a result, the energy of the absorbed photon specifies the Rydberg state produced. In contrast, specifying the energy of an incoming electron does not specify the energy of the Rydberg state produced because there is no way to control how the energy is shared between the incident electron and the electron which is excited to the Rydberg state [1]. The optical excitation

method is the most suitable way for the selective production of the specified Rydberg state.

3 Experimental Setup and Procedure

3.1 Laser Excitation and Selective Field Ionization Region

The experimental setup used in the present experiment is shown in Fig. 14. Thermal Rb atoms in ground-state are passed through the laser excitation region and then the field ionization region, which are 4 cm apart each other. The whole volume of the excitation and the field ionization regions are surrounded with three pairs of planer copper electrodes to compensate the stray field in three axis and also to apply the pulsed electric field for the ionization. The selective field ionization (SFI) electrodes consist of two parallel plates of 11 cm length and 7 cm width, in one of which a fine copper-mesh grid was incorporated into the area of 2 × 2 cm^2. The distance between the SFI electrodes is 2cm and that of other pairs of electrodes are 8 cm (for the parallel plates to the atomic beam) and 12 cm (for the perpendicular plates). The SFI electrodes and the laser interaction region were attached to a cold finger in a cryostat, thus the temperature can be varied from room temperature down to lower temperature with liquid N_2 and He.

The atoms are excited to the n Rydberg states at the laser excitation point and are ionized at the field ionization point. As the cw-lasers are used, the Rydberg atoms are produced continuously. The atomic beam is produced from an oven at about 400 K and the most probable velocity is 340 m/sec. The electrons produced by field ionization pass through the grid and are detected with a channel electron multiplier. Since the intake hole of the channel electron multiplier (called "top") is set to a high voltage ($\sim$ 300 V), all of the electrons produced by ionization at the grid portion at the moment of applying the ionization field, pass through the grid and are detected with the channel electron multiplier. The distance between the mesh wires of the grid is 1.27 mm/mesh and the mesh diameter is 0.29 mm, and thus the acceptance of the grid is $\sim$ 60 %.

3.2 Applied Pulse Shape for Field Ionization

The pulse shape applied for the SFI electrode is shown in Fig. 15. The ionization mainly occurs at the steep rise of the pulse during the time t_f, but the peak field can be kept for a time t_h (holding time) to ionize also the states with longer life time than t_f under the electric field. This point will be discussed in section 5.4. By using the waveform generator, the slew rate of the pulse can be increased up to 50 V/(cm·μsec). The applied electric field

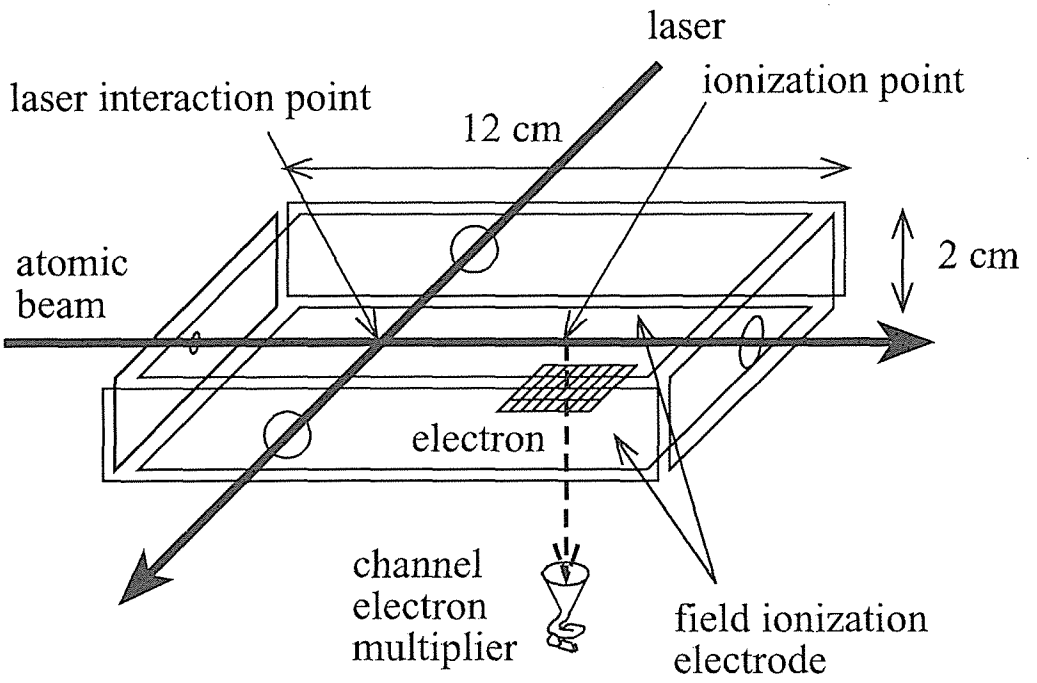

Figure 14: Experimental setup for investigating the time evolution and the field ionization process under the pulsed electric field in high slew rate regime.

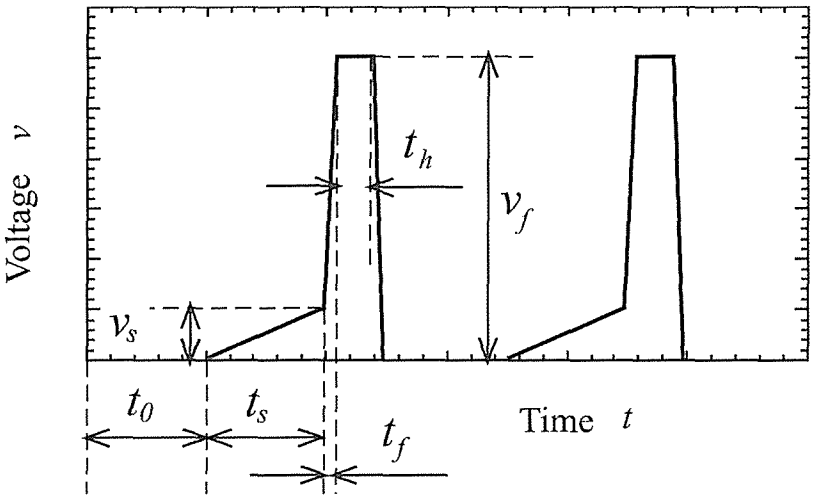

Figure 15: The pulse shape of the applied electric field.

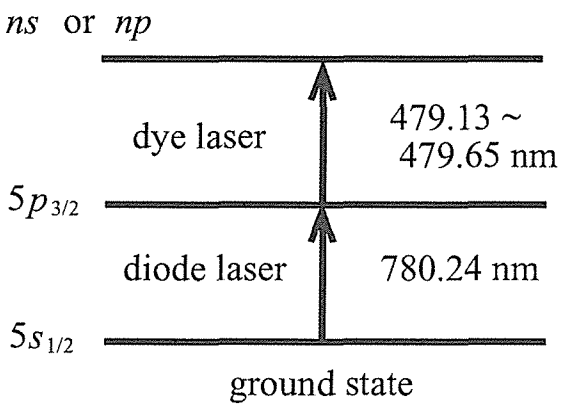

Figure 16: Excitation diagram of ^{85}Rb.

F_f is given by

$$F_f \equiv v_f/l, \tag{20}$$

where l is the distance of the SFI electrode, $l = 2$cm, and then the slew rate S_f is given by

$$S_f \equiv F_f/t_f. \tag{21}$$

The pulse has a slow component (see Fig. 15) and thus it is possible to change the slew rate by two-step in one pulse, for example, the slew rate is set low near zero field and high near the ionization threshold. This point will be discussed in section 4.3 and 5.2 in detail. The pulse sequence was produced with a waveform generator NI5411 (National Instruments). Repetition rate of the pulse was kept to 5 kHz so that the detection efficiency of the Rydberg states is optimum for the atoms with most probable velocity of 340 m/sec. Taking into account the velocity distribution of atoms and the detection efficiency in the pulsed field ionization, the overall detection efficiency is estimated to be 26 %. However the overall detection efficiency can be increased up to $\sim$ 75 % by properly adjusting the geometry of the electrodes and the pulse sequence.

3.3 Laser Setup

Two-step cw-laser excitation was adopted to excite the Rydberg nj states from the $5s_{1/2}$ ground state of ^{85}Rb through the $5p_{3/2}$ second excited states. Excitation diagram is shown in Fig. 16.

A diode laser (780 nm for the first step excitation) and a dye laser (Coherent 899-21) of coumarin 102 excited by a Kr ion laser ($\sim$ 479 nm for the second excitation) were used for the two step excitation scheme. The main

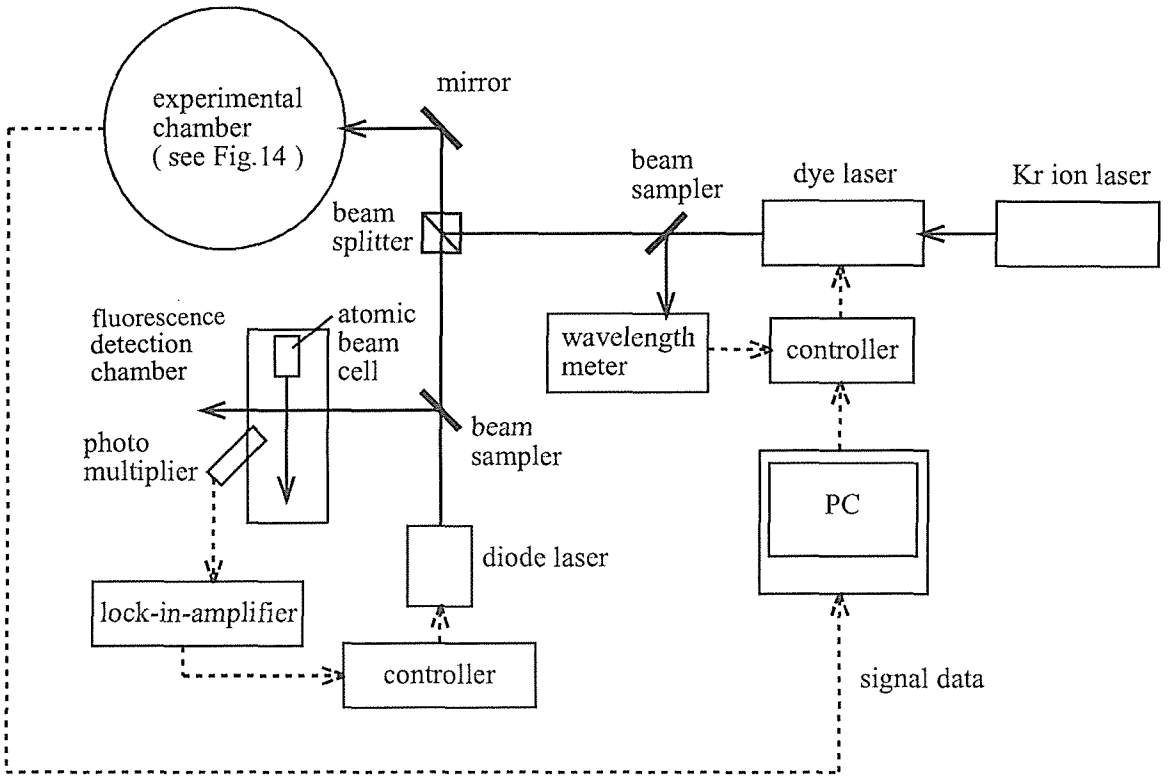

Figure 17: Schematic diagram of the optical setup.

reason to use the cw lasers to excite the Rydberg states instead of the usually adopted pulsed lasers is that we want to use this field ionization scheme for the selective ionization of highly excited Rydberg states in a *continuous* mode for the axion search experiment. The line widths of the diode laser and the dye laser are 30 MHz and 500 kHz, respectively. The power of the diode laser is 30 mW at 780 nm and that of the dye laser is 200 mW at 479 nm and at 3W of the Kr ion laser excitation.

The optical setup is shown in Fig. 17. The diode laser and the dye laser are mixed outside the experimental chamber and then injected into it. The temperature and the current of the diode laser are controlled to stabilize the wavelength. The operation values of them are -17 °C and 135 mA respectively at 780 nm. For fine-tuning and locking the wavelength, the following technique was used. A small fraction of the laser beam from the beam sampler is applied to the thermal atomic beam of Rb perpendicularly (*i.e.*, doppler free) in another chamber. The atoms are excited to the $5p_{3/2}$ state, and then decay to the $5s_{1/2}$ state again emitting the fluorescence. The

wavelength is locked to the $5s_{1/2}$ - $5p_{3/2}$ transition with a lock-in-amplifier so as to keep the fluorescence maximum by controlling and feedbacking the error signals to the diode current.

The wavelength of the dye laser is stable enough to be used for experiment for more than several minutes, even if there is no external control. In order to obtain the longer time stability further, the dye laser was also externally controlled with a PC as to be described in section 3.5.

3.4 Data Acquisition

The field ionization signals were detected and analyzed with the LabVIEW data acquisition system on a PC computer. The electron signals from the channel electron multiplier were amplified by a pre-amplifier A250 (Amptek) and a main amplifier AN302/NL (ORTEC), and then fed to a constant fraction discriminator 473A (ORTEC). The signals were counted with digital I/O channels in the data acquisition board PCI-6031E (National Instruments). The whole data was analyzed off-line as well as on-line with LabVIEW programs.

3.5 Experimental Procedure

The experiment is carried out following the procedure as follows.

1) Initial setting.
   The laser frequency (or wavelength) is set to near the objective transition (for example, the $5p_{3/2}$ - $111s$ transition) by the internal wavelength meter and controller of the dye laser.

2) Laser scanning.
   The laser is scanned in the direction of increasing frequency externally by the step of $1 \sim 5$ MHz by driving the scan-control voltage with an output from a PC and the field ionization signals are counted. During this scanning, the pulse height of the field ionization voltage (v_f in Fig. 15) is kept constant. In Fig. 18 an example of the ionization signals in the wide range of scanning in the Stark energy diagram is shown with corresponding energy levels.

3) Peak holding.
   When the peak of signals for the objective level was found, then the scan-control voltage is fixed to hold the frequency at this peak position.

4) Data taking for the ionization spectrum.
   The field ionization counts are measured by varying the amplitude

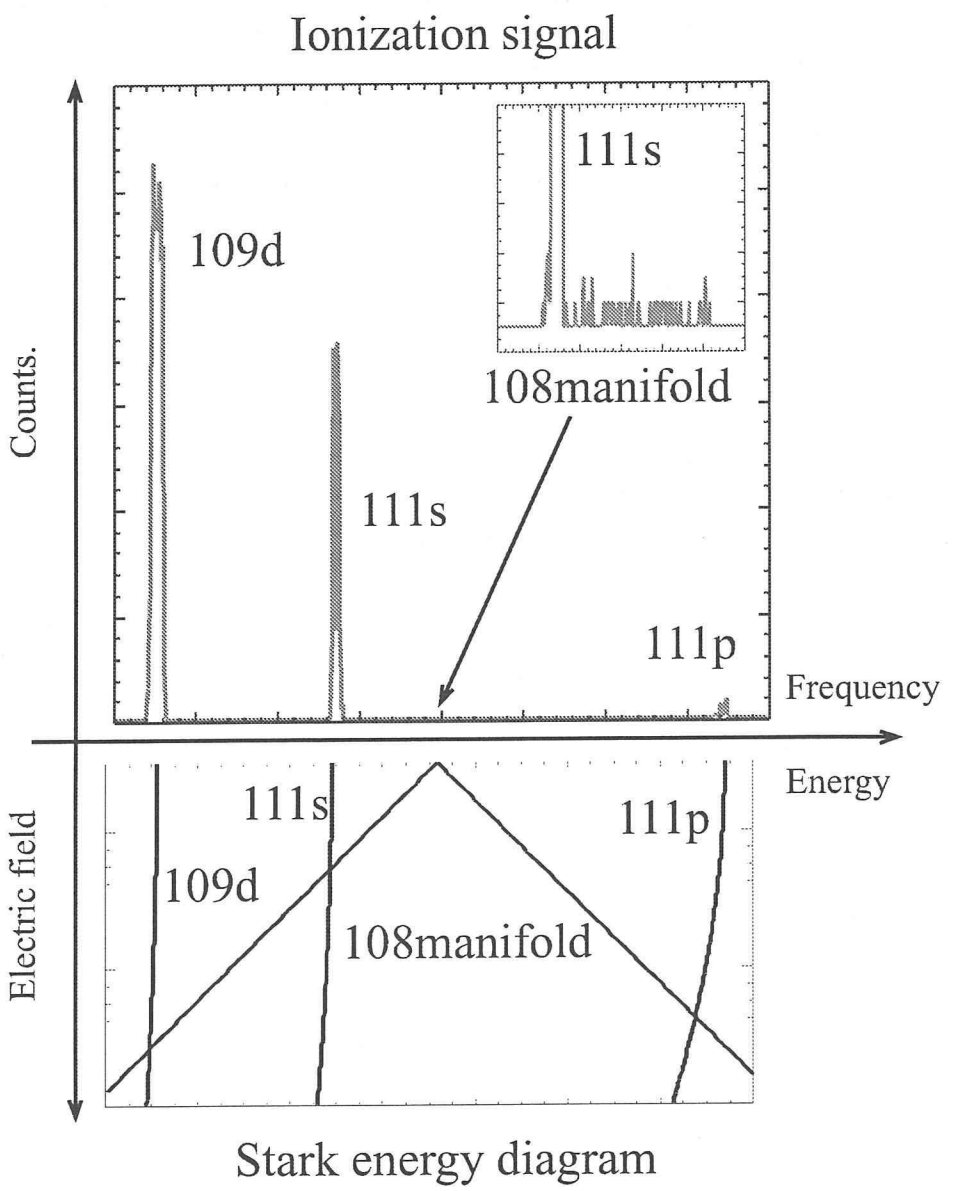

Figure 18: Ionization signals detected when the laser frequency was scanned, together with corresponding energy levels in the Stark energy diagram. The signals for 109d, 111s, 108 manifold and 111p are shown.

of the pulse v_f, while keeping v_f/t_f constant. In this process, the ionization spectrum is measured as a function of the ionization field, $F_f = v_f/l$, for a certain slew rate, $S_f = F_f/t_f$. The slow component of the pulse, v_s, is fixed to a certain value in one cycle of the data taking.

5) Re-scanning.

After several data taking for the ionization spectra, the laser is scanned again. The frequency scanning is carried out in a narrow range around the previous locking scan-control voltage following the sequence 2).

This procedure 2) - 5) is repeated for some cycles automatically, keeping thus the excitation of the Rydberg states for a long time. After the cycles, the parameters (SFI pulse shape, initial laser frequency, scanning width and etc.) are changed and the procedure is repeated. All these processes are controlled by a LabVIEW program system.

4 Results

4.1 Field Ionization Spectra

In Fig. 19 shown are typical field ionization spectra of $111p$, $111s$ and $109d$ states as a function of the applied SFI field F_f defined in Eq. 20. Fig. 19(a) - (c) show raw data observed. It is noted here that the SFI detector used in this experiment is of integral type in a sense that the field ionization signals are integrated with increasing the SFI field F_f and thus the derivative of the observed spectra with respect to the SFI field is the true counts at each bin which is shown in Fig. 19(d) - (f). The ionization threshold F_c is defined as a peak value in such derivative spectrum. These results in Fig. 19 were obtained with the slew rate S_f of the pulse (defined in Eq. 21) of 11 V/(cm·μs) and without the slow component v_s of the pulsed field. There are some important points from these spectra as follows.

1) Each spectrum has a single peak of the ionization threshold.
   Although the SFI field F_f were extended to 20 V/cm, each spectrum has only one prominent peak of the ionization threshold. Fig. 20 is a example of the spectrum shown to 20 V/cm for $111p$ state.

2) The spectra of p and s states are quite different.
   The spectra of p and s states have quite different ionization threshold and that of s and d states have the same ionization thresholds. The transitional behavior (as described later in s and p states) in the $109d$ state is also the same as in the s state.

3) The spectra of s and d have small peaks in lower field region.
   The SFI field values of these peaks are coincident with that of the ionization threshold for p state. This part of signal counts is considered to be due to the effect of blackbody radiations which induce the transition from the initial s state to the nearly p states for the reasons as described in section 5.1.

In Fig. 21 shown are field ionization spectra of $111p$ and $111s$ states as a function of the SFI field F_f, which were measured by varying the slew rate S_f of the pulse. The spectra for p state are shown in solid lines and s state broken lines, where the spectra for each state taken separately are superposed upon each other in these spectra. Here the slow component of the pulsed field v_s was set to zero.

The remarkable points observed from these spectra are as follows.

1) Each spectrum has a single peak of the ionization threshold in the wide slew rate range.

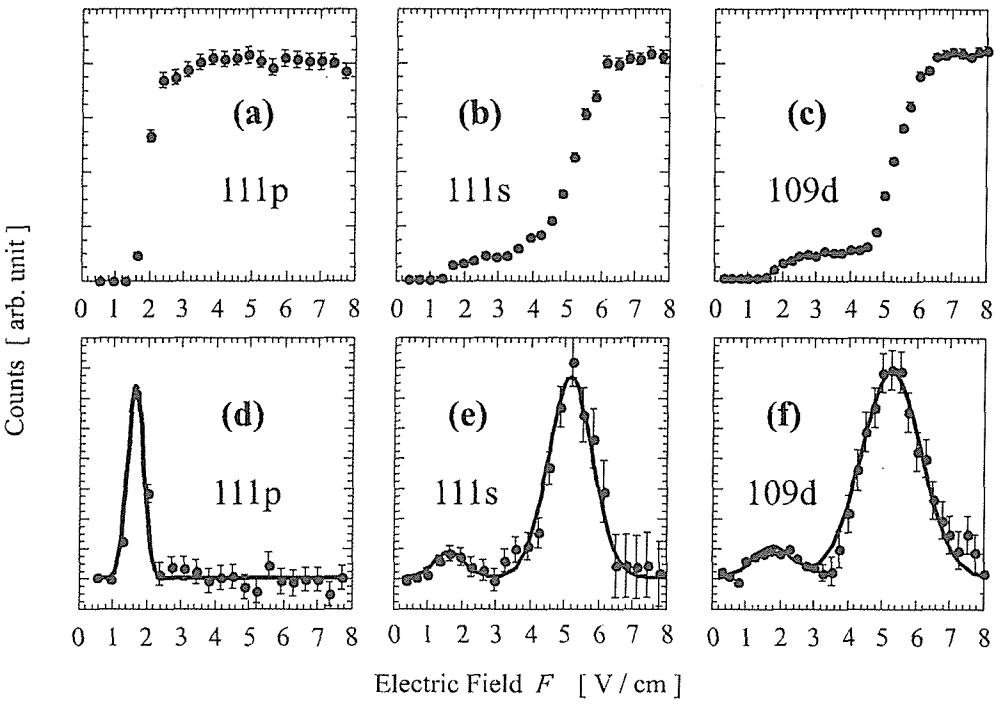

Figure 19: Typical field ionization spectra for the $111p$, $111s$ and $109d$ states; (a) - (c) show raw data observed, while (d) - (f) were obtained by taking derivatives of the raw data.

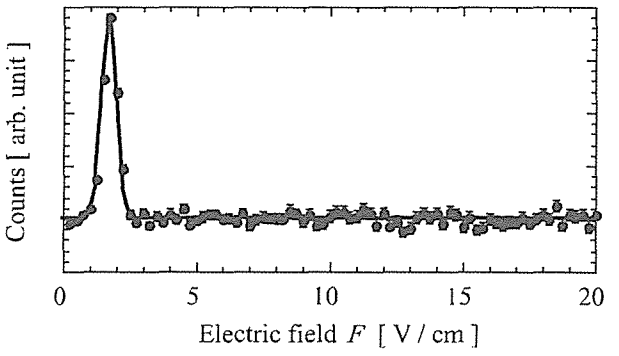

Figure 20: Typical field ionization spectrum extended to 20 V/cm of SFI field for the $111p$ state (corresponding to (d) in Fig. 19). The spectrum has only one prominent peak of ionization threshold.

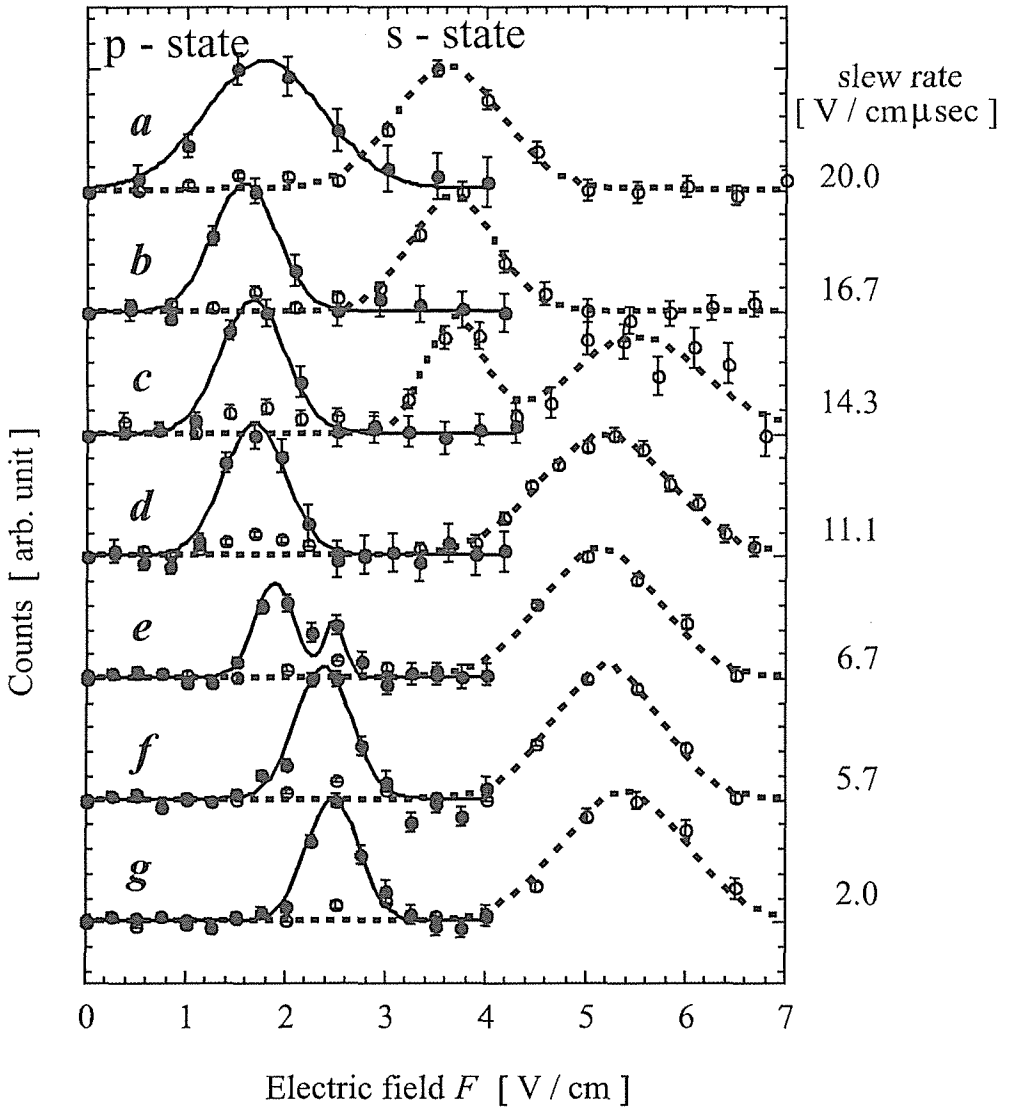

Figure 21: Field ionization spectra for the $111p$ and $111s$ states measured by varying slew rate, values of which are shown at the right side of each spectra. The spectra for each state (p and s) taken separately are superposed upon each other in these spectra. For the s state in c and the p state in e the peak width is broader, since they are in the transitional stage between two discrete ionization thresholds.

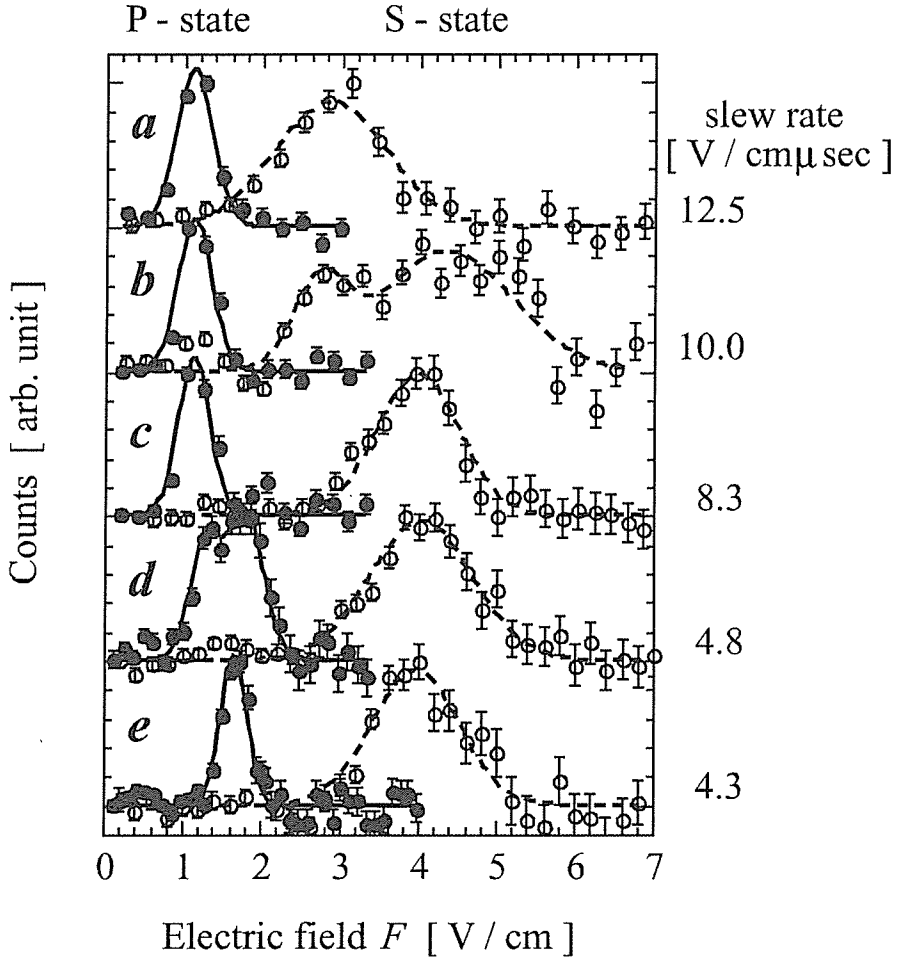

Figure 22: Field ionization spectra for the 120p and 120s states measured by varying slew rate, values of which are shown at the right side of each spectra. b and d are transitional stages for the s and p states, respectively.

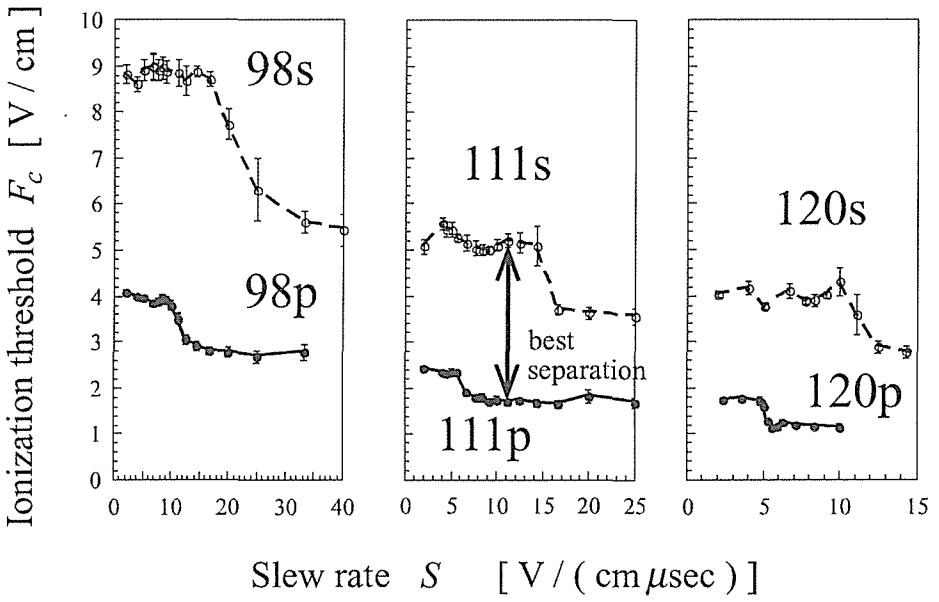

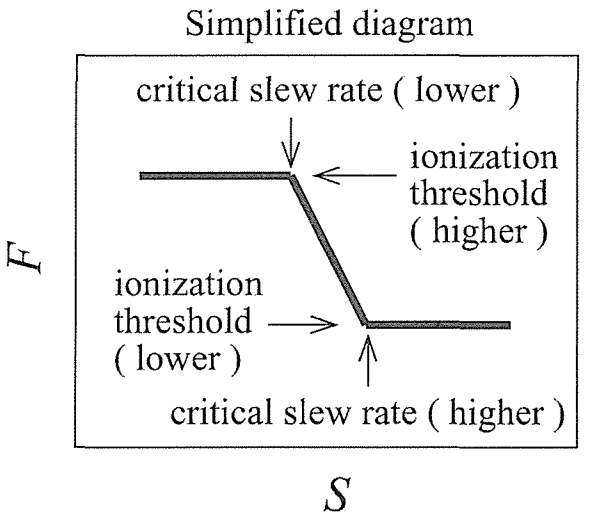

Figure 23: Slew rate dependence of the ionization threshold F_c for the $98p$, $98s$, $111p$, $111s$, $120p$ and $120s$ states, respectively. The lower and higher critical slew rates S_c are defined as the values at which the transition of the SFI field just starts to a new value and at which the transition just ends, respectively (see lower figure).

In these spectra, only one prominent peak was found as the threshold electric field except in some transitional stages (s state in Fig. 21c and p state in Fig. 21e).

2) The ionization threshold changes discretely with varying slew rate.
The SFI field value at the peak changes discretely to a smaller value at a particular slew rate with increasing slew rate. This change was observed for both the p and s states.

3) There observed some SFI signals at the lower field region ($1.2 \sim 3.0$ V/cm) in the SFI spectrum of s state.
The signal peak at this portion changed discretely with the slew rate as in the same manner as of the p state. As described above, it will be discussed for these signals in section 5.1.

1) and 2) will be discussed in section 5.3. In Fig. 22 shown are the spectra for the 120p and 120s states.

In Fig. 23 shown are the slew rate dependence of the ionization threshold F_c for the 98p, 98s, 111p, 111s, 120p and 120s states. As the slew rate increase, at first the ionization threshold of the p state goes down to the lower value and then that of the s state goes down later. In between these two transitions with the slew rate, difference in the threshold value for the two states in the field ionization becomes the largest. For example, at the slew rate of 11 V/(cm·μs) the electric field necessary to ionize the 111p state is 1.7 V/cm, while the value is 5.2 V/cm for the 111s state (shown in Fig. 23 as a comment "best separation"), then the difference is $(5.2 - 1.7)/1.7 \sim$ 200 % (corresponding to the spectra (c) and (d) in Fig. 19 and d in Fig. 21). Here the critical slew rate S_c is defined as the value at which the transition of the SFI field just starts to a new value and at which the transition just ends (see lower figure of Fig. 23). The critical slew rate for the s state is higher than that for the p state, and both of them become lower with increasing the principal quantum number n (see section 4.2).

4.2 n Dependence

In Fig. 24 shown are the n dependence of the selective field ionization (SFI) threshold F_c (as defined in section 4.1) for the p and s states. The horizontal axis is taken to the effective principal quantum number n^* ($= n - \delta_\ell$). The parameters δ_0, $\delta_2 \ldots$ in Eq. 2 for ^{85}Rb are given in Table 1 [31]. The SFI fields on the figure are those which correspond to peak position of the ionization signals. (a) and (b) in the upper figure of Fig. 24 show the higher threshold and lower threshold for the s state respectively and in a

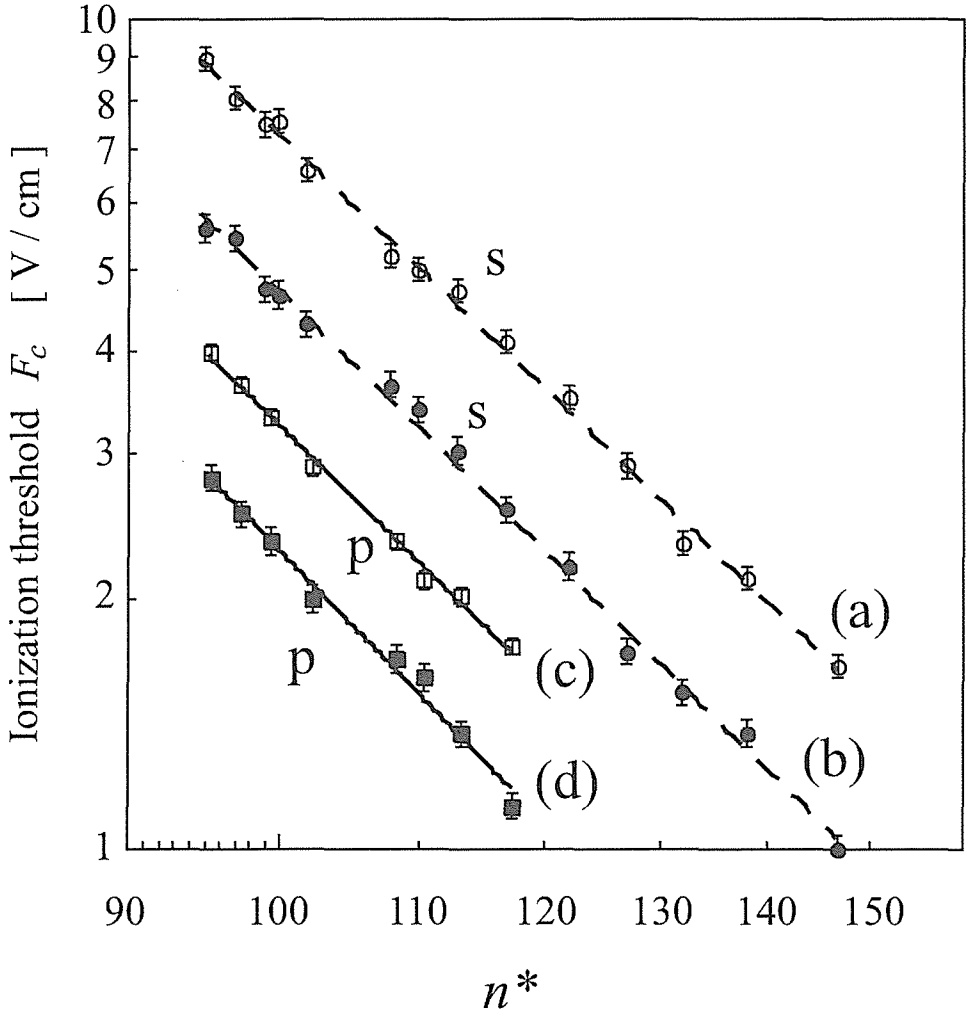

Figure 24: Dependence of the selective field ionization (SFI) threshold value F_c on the effective principal quantum number n^* in ^{85}Rb Rydberg states. Discrete two values of the SFI field observed are plotted together with the fitted lines of n-dependence. (a) and (b) show the values for the s state (broken line), and (c) and (d) for the p state (solid line). (a) and (c) show the higher ionization thresholds, and (b) and (d) show the lower thresholds (see lower figure of Fig. 23).

similar way (c) and (d) show the higher and the lower for the p state (see section 4.1 and Fig. 23). These values vary quite regularly with n ranging from 95 to 147; the SFI threshold can be well fitted to the following formula,

$$(a)F_c = (7.2 \pm 0.1) \times \left(\frac{n^*}{100}\right)^{-3.9\pm0.1} \text{ V/cm}, \tag{22}$$

$$(b)F_c = (4.7 \pm 0.1) \times \left(\frac{n^*}{100}\right)^{-4.0\pm0.1} \text{ V/cm}, \tag{23}$$

for the s state and

$$(c)F_c = (3.2 \pm 0.1) \times \left(\frac{n^*}{100}\right)^{-3.9\pm0.1} \text{ V/cm}, \tag{24}$$

$$(d)F_c = (2.3 \pm 0.1) \times \left(\frac{n^*}{100}\right)^{-4.2\pm0.2} \text{ V/cm}, \tag{25}$$

for the p state. The dependence is roughly consistent with the expected dependence of the classical ionization threshold on the energy of the levels $-2\sqrt{F}$, thus on n^{-4}.

In Fig. 25 shown are the n dependence of the critical slew rate S_c for the p and s states. The horizontal axis is taken to the effective principal quantum number n^* $(= n - \delta_\ell)$. Two kinds of the critical slew rate values as defined in section 4.1 are shown in Fig. 25. (a) and (b) show the higher and the lower critical slew rate values for the s state and (c) and (d) the higher and the lower for the p state (see section 4.1 and Fig. 23). The critical slew rate values also vary quite regularly with n. The critical slew rate are well represented by

$$(a)S_c = (23.9 \pm 1.5) \times \left(\frac{n^*}{100}\right)^{-2.8\pm0.4} \text{ V/(cm} \cdot \mu\text{sec)}, \tag{26}$$

$$(b)S_c = (15.6 \pm 0.8) \times \left(\frac{n^*}{100}\right)^{-2.8\pm0.2} \text{ V/(cm} \cdot \mu\text{sec)}, \tag{27}$$

for the s state and

$$(c)S_c = (11.3 \pm 0.3) \times \left(\frac{n^*}{100}\right)^{-3.9\pm0.2} \text{ V/(cm} \cdot \mu\text{sec)}, \tag{28}$$

$$(d)S_c = (8.2 \pm 0.2) \times \left(\frac{n^*}{100}\right)^{-3.9\pm0.2} \text{ V/(cm} \cdot \mu\text{sec)}, \tag{29}$$

for the p state.

These results indicate that this transitional behavior is quite general for a wide range of principal quantum number n and thus can be applicable to selectively ionize the p and s states for a wide range of higher excited states.

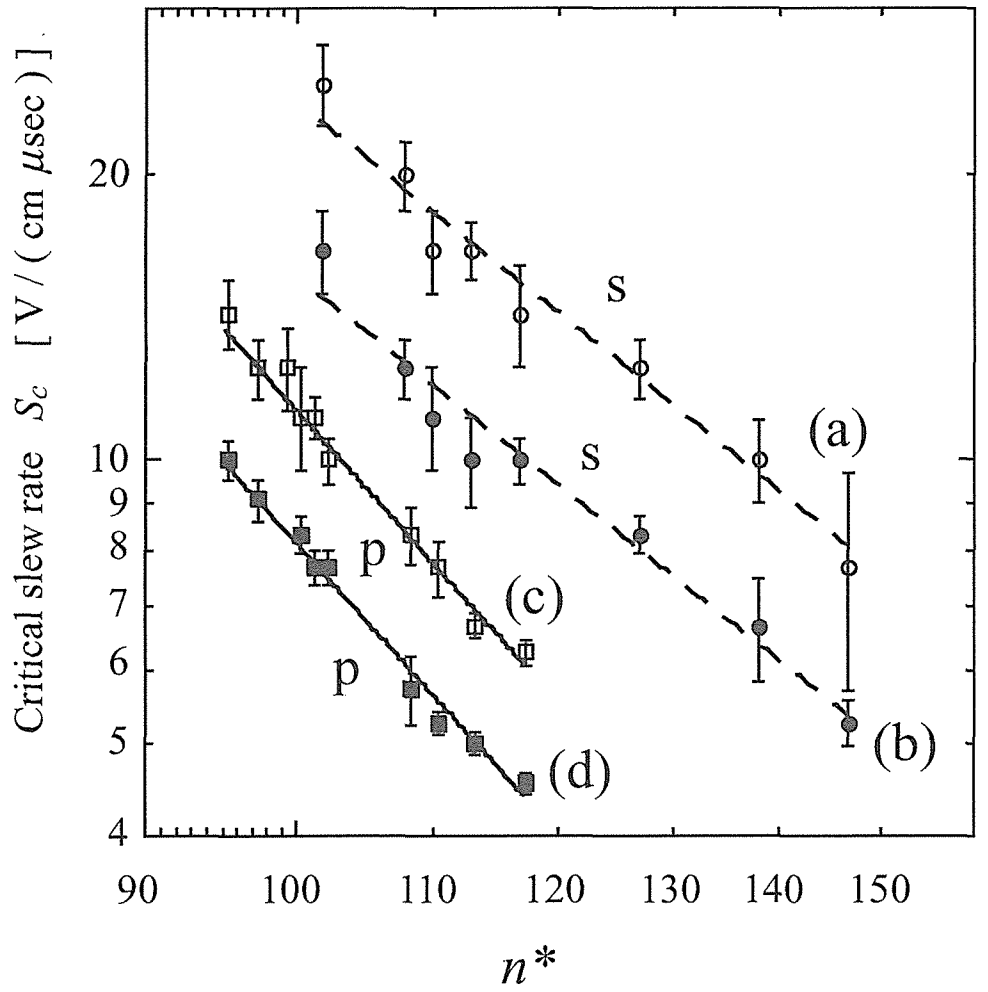

Figure 25: Dependence of the critical slew rate S_c with the fitted lines of n-dependence on the effective principal quantum number n^* in ^{85}Rb Rydberg states. (a) and (b) show the values for the s state (broken line), and (c) and (d) for the p state (solid line). (a) and (c) show the higher critical slew rate, and (b) and (d) show the lower critical slew rate (see lower figure of Fig. 23).

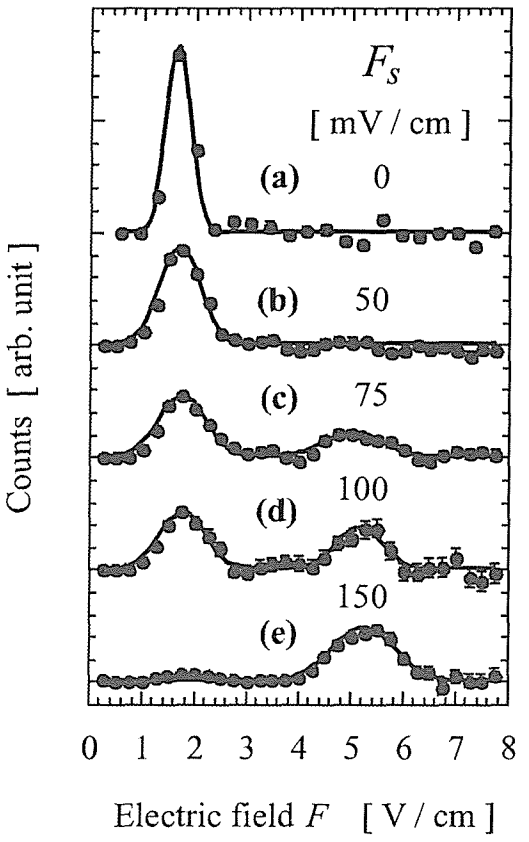

Figure 26: Field ionization spectra for the p state with increasing slow component of the applied electric field. The applied slow components F_s are 0, 50, 75, 100, 150 mV/cm, respectively from (a) to (e).

4.3 Effect of Slow Component

The above results were all obtained without the slow component v_s of the pulsed field. Switching on this value, the transitional behavior of the s state remains the same, while that of the p state changes drastically as in the following: When the applied slow component field with its slew rate less than 1 mV/(cm·μsec) exceeds the first avoided crossing field (for example, $\sim$ 75 mV/cm for the 111p state), the transitional behavior changes abruptly, becoming the same as of the s state. Example of this process is shown in Fig. 26 where the spectra for the 111p states were obtained by varying the slow component of the applied electric fields, F_s = 0, 50, 75, 100, 150 mV/cm, respectively. This field ionization behavior will be discussed in section 5.3.

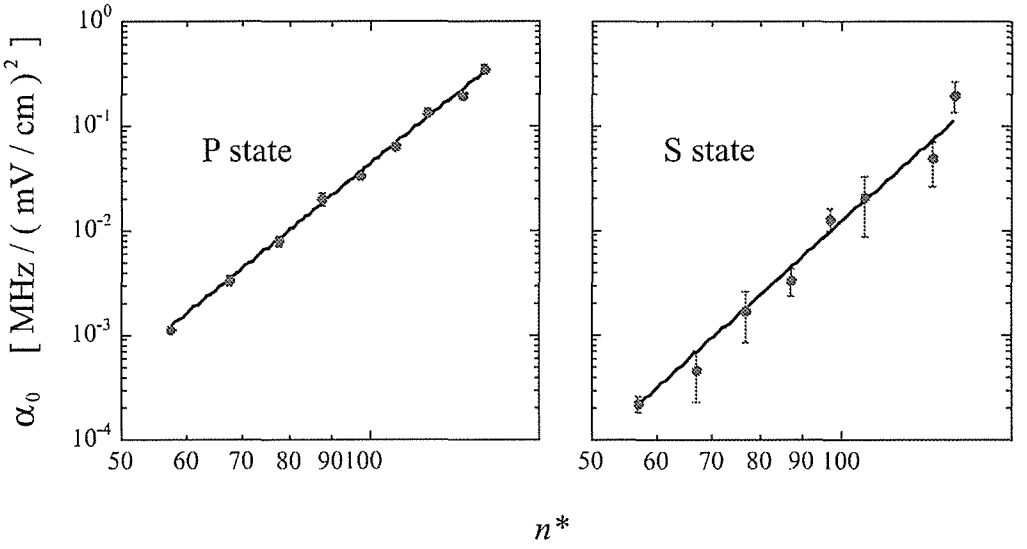

Figure 27: Measured scalar polarizabilities for the s and p states in the region of n = 60 - 150.

4.4 Stray Field

As seen in the above results, the p state was observed in this experiment in spite of the forbidden $5p_{3/2}$ - np transition in zero field. This excitation is due to the fact that there exists a stray field in the laser excitation region throughout the experiment. If there exists the stray field in the laser excitation region and its value exceeds the first anti-crossing field of the p state, the state excited will not be a pure p state, but mixed states with the manifold. During the course of the present experiment, stray field of up to 80 mV/cm was sometimes found to appear in the interaction region. In spite of the installed electrodes to compensate the stray field (see section 3.1 and Fig. 14), we did not apply any compensation potentials in such cases, but always renewed the SFI electrodes to keep the stray field less than about 15 mV/cm in the interaction region. This is because any static field applied for compensation may affect the experimental observations as actually verified as above. In the observed stray field, the p state with n less than 120 is well separated from the adjacent manifold levels.

The stray field in the laser excitation region were determined by measuring the level distance between the s and p states in the laser frequency scanning process (see section 3.5 and Fig. 18). We measured the scalar polarizabilities for the s and p states in Eq. 12 in another experimental setup

[35]. Taking these parameters and Eq. 12 into account, the electric field in the laser excitation region is calculated from the level distance. In Fig. 27 shown is the results of the measurement of the scalar polarizabilities in the region of $n = 60$ - 150. The detailed discussion on the results will be reported elsewhere [35].

5 Discussion

5.1 Selectivity in the Field Ionization

As described in Introduction, the first purpose in this experiment is to establish a way to detect such higher excited states selectively with the pulsed field ionization method. The separation between the ionization thresholds for the p and s states should be maximized in the selective field ionization. As seen in section 4.1 and in Fig. 23, the separation becomes quite large by selecting the optimum slew rate. For example, the difference in the ionization field is $\sim$ 200 % for the p and s states, quite large compared to the case of adiabatic transition in which the difference would be only 5 % for the states at $n \sim 110$.

It should also be noted here that the transitional behavior in the $109d$ state is similar to that in the s state as mentioned above (see section 4.1 and Fig. 19). This result indicates that the transitional behavior depends on the energy position of the states relative to the adjacent manifold. The upper positioned state p (see Fig. 4) shows different transitional behavior from the lower positioned s and d states. Here the *upper – side* levels are referred to the state with the quantum defect value $|\delta|(\mathrm{mod}\ 1) \geq 0.5$.

Related to the selectivity in the Rydberg states, it should be noted that there observed some SFI signals at the lower field region (1.2 $\sim$ 3.0 V/cm) in the SFI spectrum for the s state (see section 4.1, Fig.19, and Fig.21). The signal peak at this portion changed discretely with slew rate as in the same manner as of the p state. This part of signal counts is considered to due to the effect of blackbody radiations which induce the transition from the initial s state to the p states. In fact the counts at this portion measured by varying the temperature of the excitation-detection region from 120 K to 40 K was found to depend linearly on the temperature as expected. In Fig. 28 shown is the temperature dependence of the ratio of the SFI signal at the lower field region to the total signal in the SFI spectrum for the $111s$ state. The observed transition rate to the p state is in roughly agreement in its absolute values and in good agreement in its temperature dependence with the theoretical predictions. This agreement indicates also that the selectivity of the excited states with the field ionization method in the pulsed electric field regime is quite good even at such highly excited region. The detailed discussion on the s to p transitions and the effect of blackbody radiations will be reported elsewhere [36].

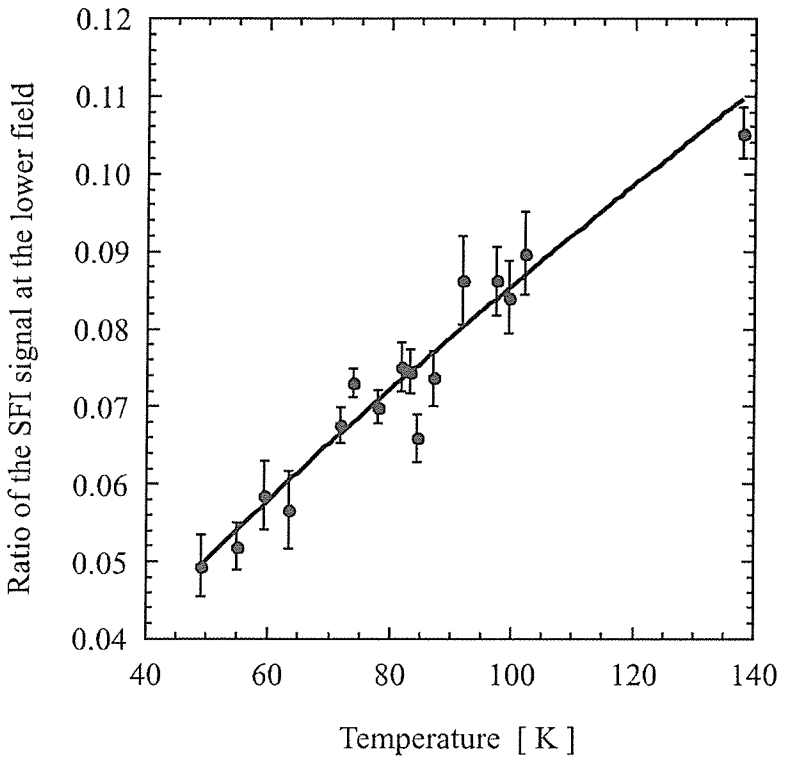

Figure 28: Temperature dependence of the ratio of the SFI signal at the lower field region to the total signal in the SFI spectrum for the $111s$ state (see text in detail for the meaning of "the SFI signal at the lower field".)

5.2 Effect of Slow Component in Pulsed Electric Field

In Fig. 29 shown is the Stark energy diagram near the 108 manifold in ^{85}Rb. In the upper figure the whole diagram including the ionization region is shown and the lower one is an expanded diagram for the region of low electric field. The arrows indicate the possible trajectories for the "purely adiabatic" (2 and 3) and the "purely diabatic" (1 and 4) (see section 2.3). To achieve the best separation in the ionization field between the p and s states, the trajectory 1 for the p state and 4 for the s state are preferable. According to the simple argument in section 2.3, in order to trace the trajectory 1, it is expected that the slew rate is low enough at the first avoided crossing (indicated by a circle) and extremely high at all other crossings. In the case of the $111p$ state, then the value of the slow component v_s of the applied field ionization pulse should be located between 75 mV (the first crossing) and 110 mV (the second crossing). In the actual situation, however, the ionization spectrum of the $111p$ state was the same as that of the $111s$ state in the condition described above. This result indicates that once the first anti-crossing is traversed adiabatically and the state is mixed with the adjacent manifold levels, then the following SFI behavior for the p state under the high slew rate regime changes completely, resulting no difference in their behavior between the states of opposite positions to the adjacent manifold.

5.3 Ionization Threshold

As described in section 4.1, the ionization spectrum has only one prominent peak and the ionization threshold changed discretely to a smaller value with increasing slew rate for both the p and s states. The peak field does neither correspond exactly to the expected position from the purely adiabatic (paths 2 or 3 in Fig. 29), nor the purely diabatic transitions (paths 1 or 4) leading to the reddest or bluest trajectory in the adjacent manifold; the expected fields for these paths (1 to 4) in $n = 108$ (corresponding to the adjacent manifold of $111s$ and $111p$ states from the quantum defect values in Rb) are 1.8, 2.4, 2.4, and 4.2 V/cm respectively, which should be compared to the observed field values of 1.7 and 5.2 V/cm for the p and s states, respectively.

This behavior is quite different from those of the previous experiments for the lower n Rydberg states ($n < 70$) in pulsed electric field (sodium in [25,26,27,28], potassium in [29], indium in [30]). The ionization spectra in these experiment were found to change continuously with increasing slew rate and have multiple peaks distributed continuously between the "purely adiabatic" and the "purely diabatic" peaks (see Fig. 5 and 12).

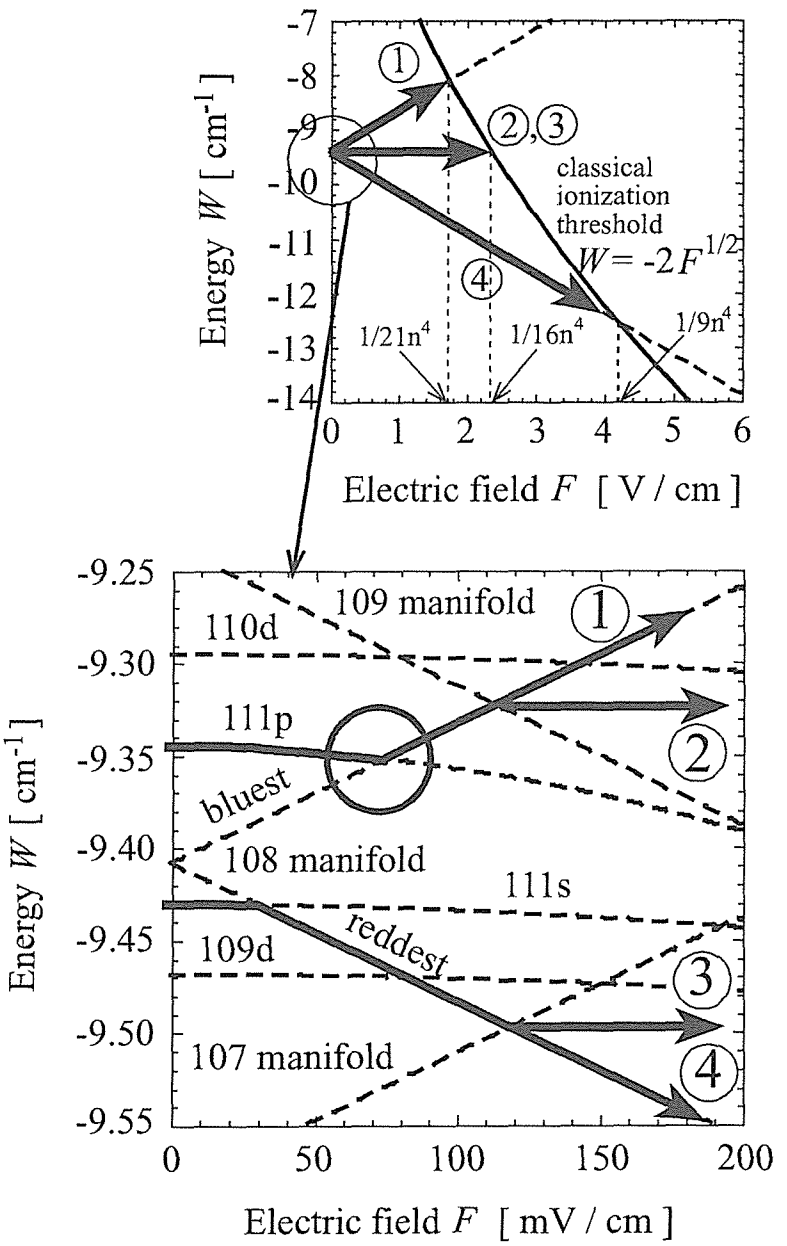

Figure 29: Stark energy diagram near the 108 manifold in ^{85}Rb. The arrows 1 to 4 indicate the possible trajectories for the "purely adiabatic" (2 and 3) and the "purely diabatic" (1 and 4) transitions.

5.4 Effect of Holding Time

In hydrogenic atoms the blue states of manifold have long lifetime as described in section 2.3. Thus to check whether the behavior of the blue states is hydrogenic or non-hydrogenic, the SFI have to be examined up to the long lifetime regime. The decay rate Γ of the blue states in the electric field by the tunneling process, estimated from the hydrogenic approximation, is given by

$$\Gamma = \frac{(4R)^{2n_2+m+1}}{n^3 n_2!(n_2+m)!} \times \exp\left(-\frac{2}{3}R - \frac{n^3F}{4}\left(34n_2^2 + 34n_2m + 46n_2 + 7m^2 + 23m + \frac{53}{3}\right)\right), \quad (30)$$

where $R = (-2W)^{3/2}F^{-1}$ (cited from Ref.[37]). For $n \sim 111$ the decay rate is much higher than 5×10^3 s^{-1}. Since the applied SFI pulse can hold the electric field F_f during the time t_h (see Fig. 15), it is possible to observe possible contributions of the levels with long lifetime in the pulsed electric field. The SFI spectra observed with the holding time t_h extended up to 200 μs showed no distinguishable difference from those taken with the short holding time of 1 μs, indicating all the states ionized have decay lifetime shorter than 1 μs in the electric field. Also we observed no significant SFI-signals over 20 V/cm in the spectra measured as described in section 4.1 (see Fig. 20). Therefore the ionization process for the states along the blue line (trajectory 1 in Fig. 29) is not due to the tunneling process but of autoionization-like one due to their mixing to the red continuum, even though such coupling becoming weaker as n increases [1].

5.5 Incoherent Process

These experimental results for the transitional behavior described above are in general not in agreement with simple predictions from the incoherent contributions of adiabatic and non-adiabatic transition processes. First, consider a model calculated by Harmin and Price [38] for the incoherent process to compare with the experimental results. In the model the mixing of Rydberg manifolds, induced by a ramped electric field ($S = dF/dt$ =constant), is modeled by interactions among two intersecting groups of parallel energy levels. The levels form a grid, each node of which is treated as an isolated two-level Landau-Zener anticrossing, characterized by the diabatic transition probability D.

In Fig. 30 shown is the Landau-Zener grid in the model calculated by Harmin and Price. The left figure shows the Stark energy diagram for the n

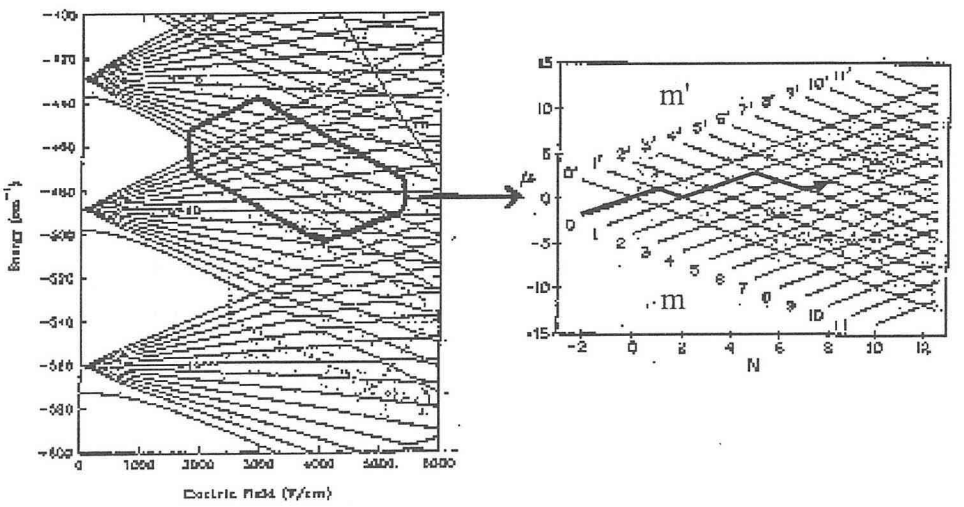

Figure 30: Landau-Zener grid in the model calculated by Harmin (cited from Ref.[38]).

and $n+1$ Rydberg states and the right figure shows the Landau-Zener grid of identical anticrossings formed by two interacting manifolds of parallel energy levels. The right figure shows the detail in the area indicated with solid line in the left figure. Up- and down-going levels are labeled $m = 0, 1, \ldots$ and $m' = 0', 1', \ldots$, respectively. Generation number $N = m + m'$ is proportional to the electric field and thus to the time, and vertical scale $\mu = m' - m$ is proportional to intersection energies. In the bluest level of the n manifold ($m = 0$ line), taking into $n_1 - n_2 = n - 1$ account in Eq. 9, the level slope dW_1 in Eq. 13 is give by

$$\frac{dW_1}{dF} = \frac{3}{2}n(n-1). \tag{31}$$

And in the reddest level of the $n+1$ manifold ($m' = 0'$ line), taking into $n_1 - n_2 = -(n+1)$ account in a similar way,

$$\frac{dW_2}{dF} = -\frac{3}{2}n(n+1). \tag{32}$$

Taking the isolated avoided crossing of magnitude ω_0 between two levels as $\sim |\delta|/n^4$ [38], the diabatic transition probability D in Eq. 14 is given,

$$D = \exp\left(-2\pi\frac{|\delta|^2}{3Sn^{10}}\right), \tag{33}$$

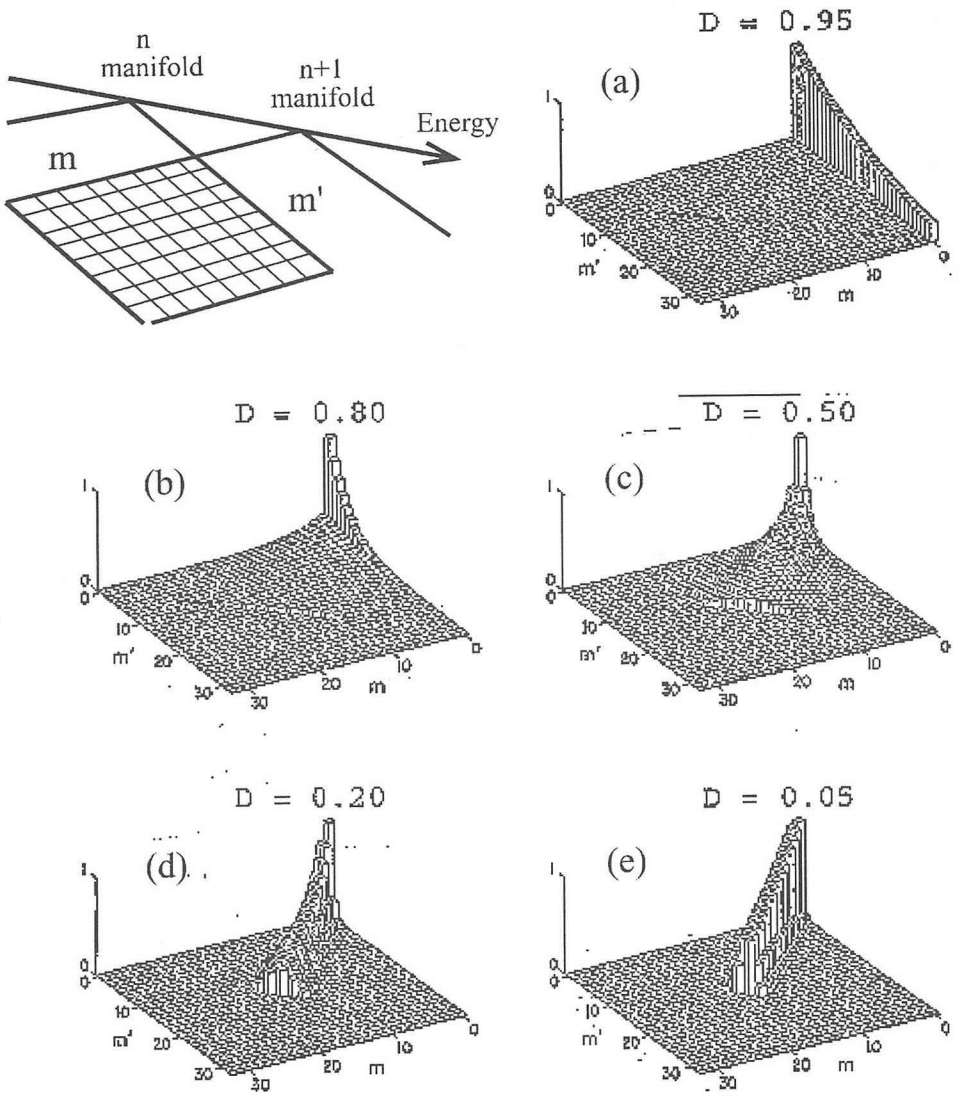

Figure 31: Calculated probability of arriving at intersection $[m,m']$ on a Landau-Zener grid in the coherent process (cited from Ref.[38]) with the diabatic transition probability D.

and the adiabatic transition probability $A = 1 - D$. In the case of slew rate $\sim$ 20 V/(cm·μsec) at $n \sim 100$, the probability of diabatic transition D is quite high, reaching $\sim$ 99.8%.

In the incoherent time evolution, a transition probability for a certain avoided crossing is calculated independently of interactions from other crossings. For example, the total transition probability for the trajectory indicated as an arrow in the right figure of Fig. 30 is given by, $D \cdot A \cdot A \cdot D \cdot D \cdot A \cdot D \cdot A \cdot = D^4 A^4$. Since the energy levels are in parallel and the slew rate is assumed to be constant, D and A are constant at all the avoided crossings.

In Fig. 31 shown is the probability of arriving at intersection $[m, m']$ on a Landau-Zener grid calculated by Harmin and Price [38]. The initial level is the bluest level of the n manifold ($m = 0$). In the case of higher diabatic transition probability (see (a)), the probability distributes along the bluest level ($m = 0$), *i.e.*, it approaches the purely diabatic trajectory described above, and in the case of lower diabatic transition, it distributes around the center of the diagram ($m = m'$), *i.e.*, the purely adiabatic trajectory.

We calculated the ionization spectra further in detail [39] based on the Landau-Zener formula. In this calculation the actual energy levels of ^{85}Rb were taken into account by assuming each crossing to be isolated. The transitions at each crossing was evaluated with a Monte Carlo simulation method. Thus the time evolution behavior of ^{85}Rb Rydberg states calculated here is much more realistic than the simple model describe above. In Fig. 32 shown are the expected ionization spectra with the model. The figures (a) - (c) show the spectra for the bluest state in $n = 108$ manifold with $D = 0.999, 0.99, 0.9$, and (d) - (e) for the reddest state, respectively. According to the calculation,

1) only in the extremely high slew-rate case, $D = 0.999$, the spectrum has a single and sharp peak for each state and the bluest and the reddest states have well separated threshold values in field ionization,

2) the ionization spectra continuously vary with decreasing slew rate,

3) and with increasing slew rate, the ionization threshold for the bluest state becomes lower, while that for the reddest state becomes higher.

Contrary to these predictions, the ionization thresholds for both the p and s states were found to change discretely in the present experiment and become lower with increasing slew rate.

Considering the above discrepancy between the observed ionization behavior and the predictions based on the incoherent process, more refined treatment for the field ionization processes have to be invoked. In the next section therefore the effect of coherent time evolution will be considered,

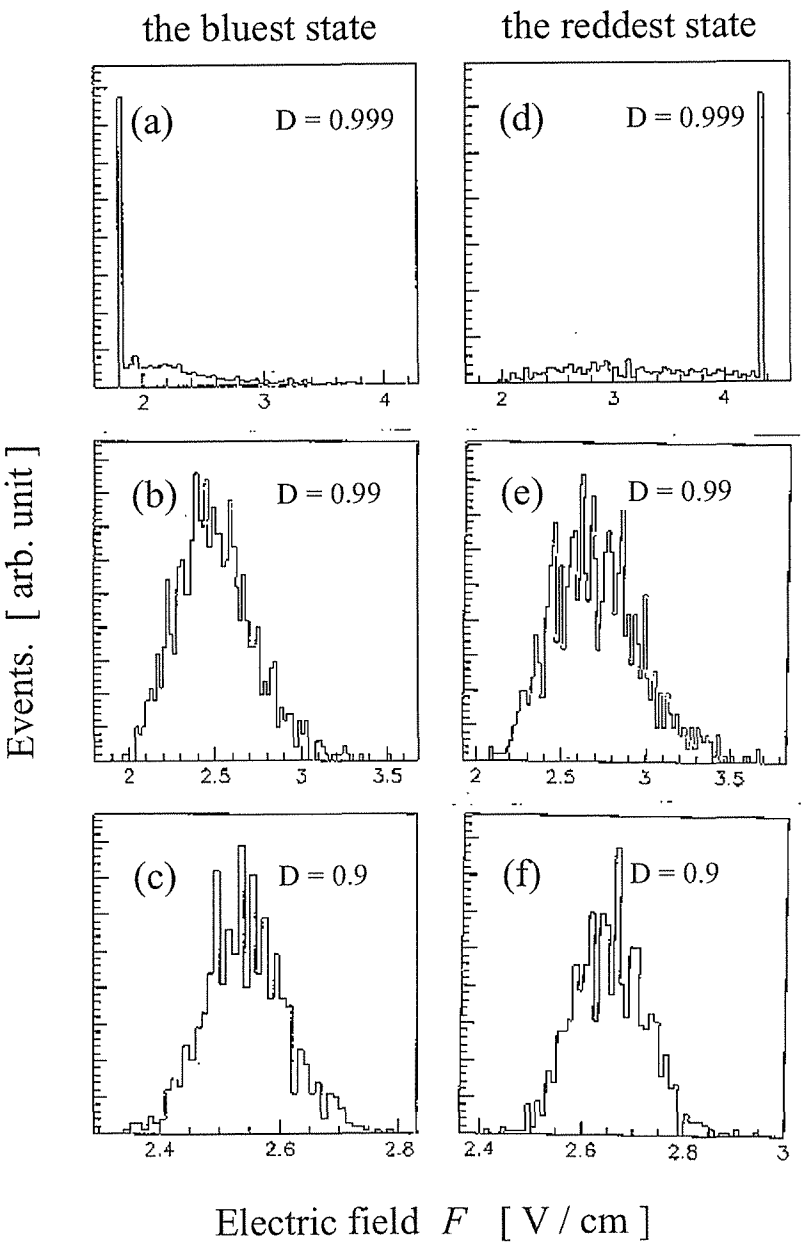

Figure 32: Calculated ionization spectra [39] in the conditions for $D = 0.999, 0.99, 0.9$ and $n = 108$. In this calculation the actual energy levels of ^{85}Rb were taken into account by assuming each crossing to be isolated and the transitions at each crossing was evaluated with a Monte Carlo simulation method: (a) -(c), the spectra for the bluest state, (d) - (f), the spectra for the reddest state.

since many number of Stark levels are excited along the applied electric field and these energy levels experience the enormous number of the Stark level crossings up to the time to be ionized.

5.6 Coherent Time Evolution

Following the work for the incoherent process, Harmin [23] examined coherent time evolution on a grid of Landau-Zener anti-crossing under a linear ramped electric field in which each manifold levels are treated as linear in time, parallel, and equally spaced and infinite number. The time development of an initially populated state is then governed by two level Landau-Zener transitions at avoided crossings and adiabatic evolution between them. In the treatment he kept the Landau-Zener approximation but restored interference effects to describe coherent time evolution. The key parameters in this model study are 1)the Landau-Zener transition probabilities D for making a diabatic transition process at the avoided crossing traversals and 2) the dynamical phase unit φ. The phase unit φ is the area covered by the pair of the adjacent up- and down-going levels. In coherent process the parameters d and a, which are the diabatic and adiabatic transition matrix elements, respectively, have to be taken into account coherently. Here the parameters d and a are given by

$$d = \exp\left(-\pi \frac{|v_{mm'}|^2}{|p - p'|}\right), \tag{34}$$

$$a = (1 - d^2)^{1/2}, \tag{35}$$

where $v_{mm'} = \langle m|\hat{H}|m'\rangle$ is an interaction between two intersecting energy levels m and m' and p, p' are the level slopes. Then D and A are represented by $D = d^2$, $A = a^2 = 1 - D$.

In Fig. 33 shown is the Landau-Zener grid in the model calculated for the coherent time evolution (cited from Ref.[23]). In the left figure of Fig. 33 shaded area shows a dynamical phase unit φ and in the right figure two interfering paths from the initial level $m = 0$ at intersection $[0, 0']$ to up-going level $m = 4$ at intersection $[4, 6']$ (with regard to the notation of m and m', see section 5.5). The solid arrow shows one of possible paths j from $[0, 0']$ to $[4, 6']$. The path has area 17φ (shaded), and its amplitude of wavefunction is $-d^4a^6e^{i17\varphi}$. It is noted that d and a are summed up in the coherent process, while D and A are summed up in the incoherent process. The broken arrow shows another path j'. It has area 12φ (shaded) and its amplitude is $-d^8a^2e^{i12\varphi}$. The difference of their actions $\int dt[W_{j'}(t) - W_j(t)] = 5\varphi$ is the net area enclosed by the loop formed by paths j and j'. The total amplitude

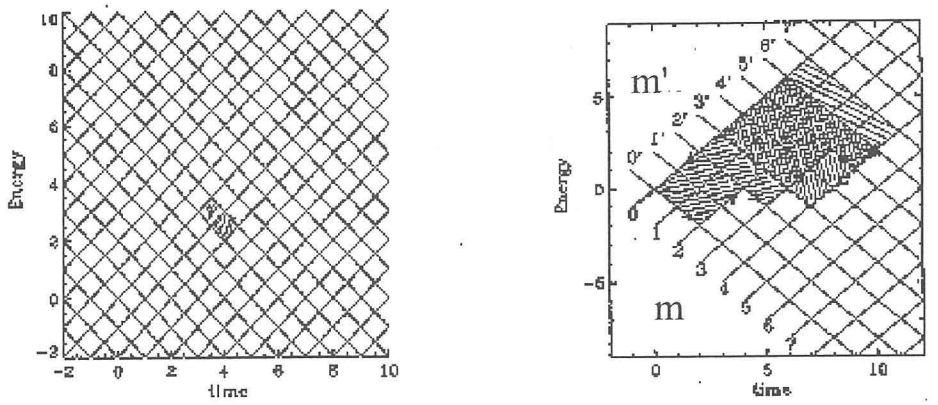

Figure 33: Landau-Zener grid in the coherent model (cited from Ref.[23]).

$A_{mm'}(d,\varphi)$ for all paths from $[0,0']$ that arrive at $[m,m']$ is given by

$$A_{mm'}(d,\varphi) = \sum_j |C_j(t^-_{mm'})|(-1)^{u_j} \times \exp\left(i\int_{t_{00'}}^{t_{mm'}} dt[W_0(t) - W_j(t)]\right), \tag{36}$$

where $C_j(t)$ is the amplitude for each path as function of time. The total probability $P_{mm'}(d,\varphi)$ is then given by summing up all the relevant amplitudes coherently,

$$P_{mm'}(d,\varphi) = \sum_j \sum_{j'} |C_j(t^-_{mm'})C_{j'}(t^-_{mm'})|(-1)^{u_j+u_{j'}} \times \exp\left(i\int_{t_{00'}}^{t_{mm'}} dt[W_{j'}(t) - W_j(t)]\right), \tag{37}$$

where $|C_j(t^-_{mm'})|$ is a product of $m+m'$ factors of d's and a's, and u_j is the number of up-to-up traversals of avoided crossings along path j [23].

During an interval $t_1 \leq t \leq t_2$, any two distinct paths between $[m_1,m_1']$ and $[m_2,m_2']$ will accumulate dynamical phases that interfere as gauged by the phase difference

$$\Delta\Phi = \int_{t_1}^{t_2} dt\Delta E(t) \tag{38}$$

for the two paths. This overall difference in phase advance $\Delta\Phi$ for two paths from zero to the ionization field is equal to the sum of the phase units φ in

the whole area covered by the two paths. In the actual Stark energy-field grid system, the phase units φ_i are not a constant but vary with respective anti-crossings i. In this equally-spaced model, φ is estimated approximately by

$$\varphi \sim \frac{1}{3Sn^{10}}, \tag{39}$$

where S is the slew rate of the applied electric field F, and d is given by

$$d = \exp(-\pi\tilde{\delta}^2\varphi) \tag{40}$$

where $\tilde{\delta}$ is an average low-ℓ quantum defect.

The probability D increases monotonically with increasing slew rate, while the overall difference in phase advance $\Delta\Phi$ of the state wavefunction through the grid is effective in modulo 2π and strongly affects the coherent nature of the process through the interference between many states populated along the way of traversals in the applied electric field [23].

In Fig. 34 shown are the contour plots of total probabilities $P_{mm'}(d,\varphi)$ for totally constructive interference $\varphi = 0(\mathrm{mod}2\pi)$ and various values of the diabatic transition probability $D = d^2$ (cited from Ref.[23]). The initial level is up-going state, $m = 0$ at the intersection with $m' = 0$. Since $\varphi = 0(\mathrm{mod}2\pi)$, all the relevant wavefuntions are in pase, and thus the coherent effect is observed most clearly. In the case of highly diabatic transition probability (see (e)), the probability distributes along the bluest level ($m = 0$), *i.e.*, it approaches the purely diabatic trajectory, and in the case of low diabatic transition probability (see (e)), it distributes around the center of the diagram ($m = m'$), *i.e.*, the purely adiabatic trajectory.

In Fig. 35 shown are the three-dimensional and contour plots of total probabilities $P_{mm'}(d,\varphi)$, for fixed $\varphi = \pi/4$ and larger values of the diabatic transition probability $D = d^2$ (cited from Ref.[23]). With the diabatic transition probability approaching 1, from (a) to (c) in Fig. 35, $P_{mm'}(d,\varphi)$ becomes markedly asymmetric, peaking preferentially along loci of levels nearly parallel to one another and to the original $m = 0$ level, thereby forming "*resonance lanes*" on the grid [23].

In the present experimental setup with slew rate ~ 20 V/(cm·μs) at $n \sim 100$, the probability of diabatic transition D is quite high, reaching $\sim 99.8\%$ from the above estimation so that our case corresponds to the diabatic limit in Harmin's treatment in a good approximation.

Taking the quantum defect values of low ℓ states into account, estimated phase unit φ varies from 10^{-2} to 10^{-3} with increasing electric field. The number of avoided crossings traversed between zero field and the field ionization region in Rb is estimated to be $N_{blue} \sim 900(n/100)^2$, $N_{red} \sim 1150(n/100)^2$

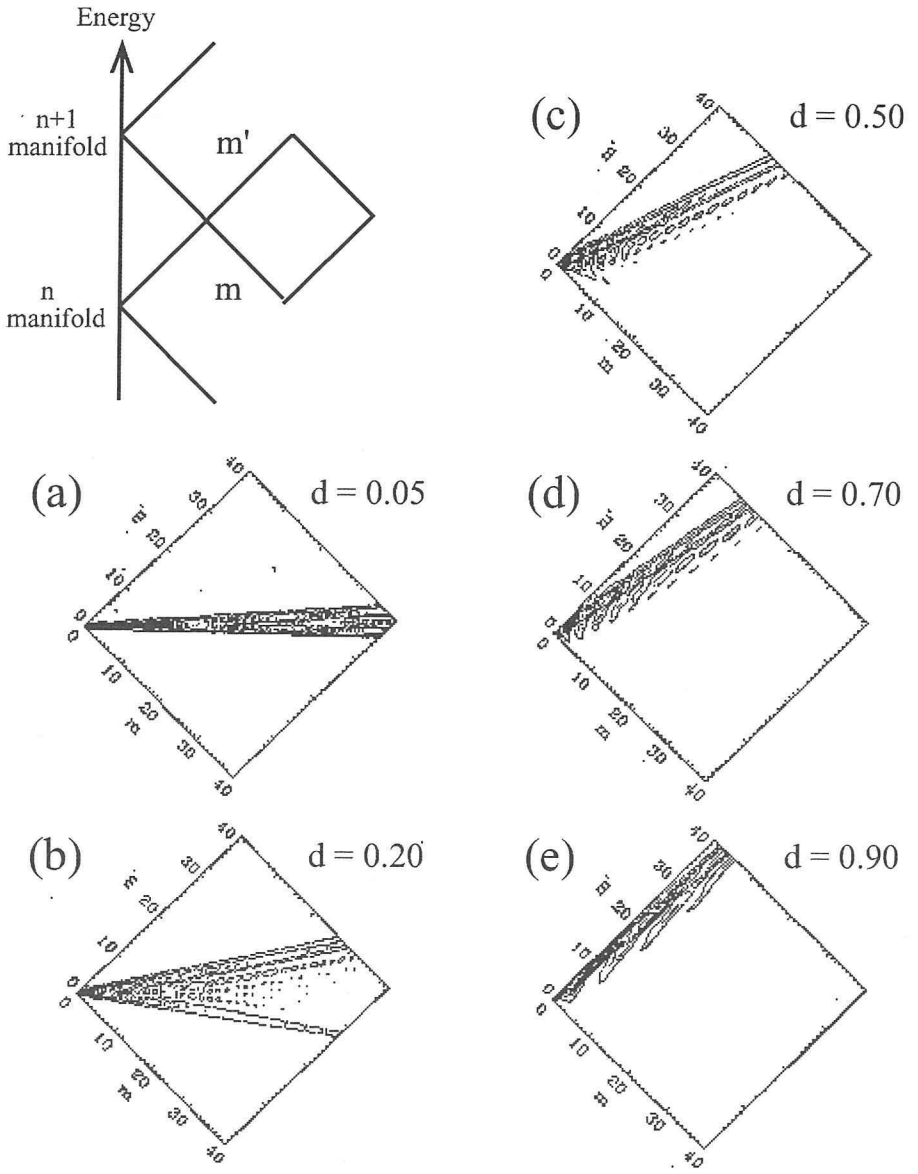

Figure 34: Contour plots of total probabilities $P_{mm'}(d, \varphi)$ (cited from Ref.[23]) for totally constructive interference $\varphi = 0(\mathrm{mod}2\pi)$. (a) $d = 0.05$, (b) 0.20, (c) 0.50, (d) 0.70 and (e) 0.90.

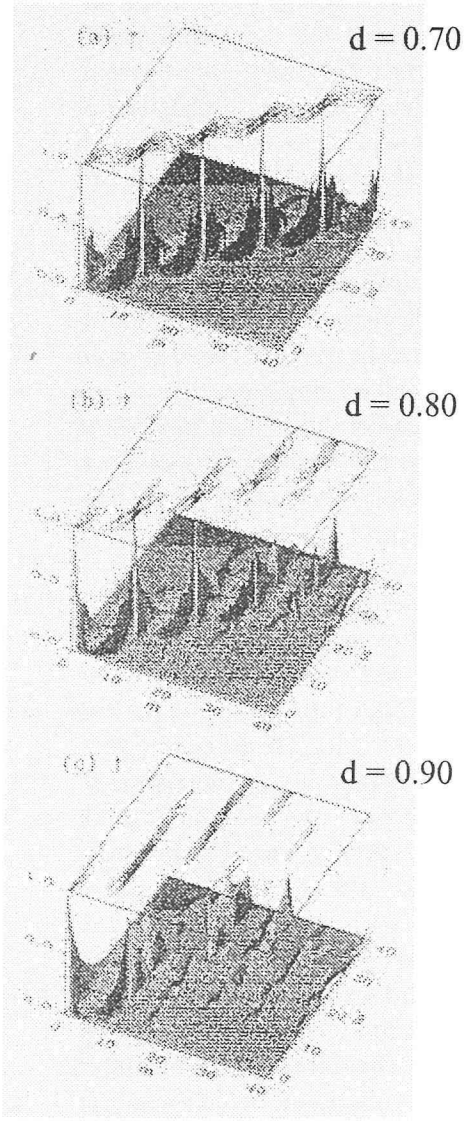

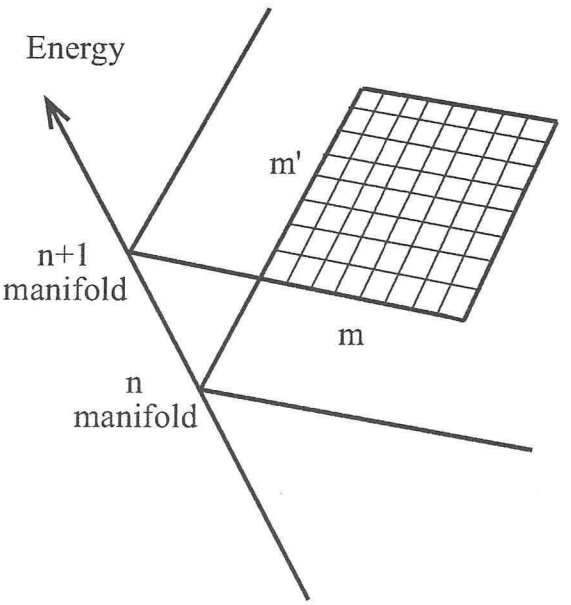

Figure 35: Three-dimensional and contour plots of total probabilities $P_{mm'}(d, \varphi)$, for fixed $\varphi = \pi/4$ and larger values of the diabatic transition probability $D = d^2$ (a) - (c): (a) $d = 0.70$, (b) 0.80, (c) 0.90 [23].

for the up- (bluest) and down- (reddest) going trajectories, respectively. At the region of $n \sim 110$, this number of anti-crossing traversals suggests that the phase advance is over 2π at some field value. When this resonance condition is fulfilled, the constructive interference between the many number of Stark states along the advance of the pulsed electric field may result in one prominent peak in the sfi field. In Harmin's analysis [23], the population of the states under the electric field was found to make a series of resonances in a form of *lanes* along the up- or down-going directions of the initially excited state at zero field.

This general feature in the diabatic limit seems to be satisfied experimentally, since a discrete sequence of SFI threshold field was found, depending on the slew rate. However there is a significant difference in the experimental observations compared to the model calculation in that the observed SFI field values for both the s and p states decrease with increasing slew rate. Contrary to this observation, the model calculation predicts that with increasing slew rate, the most populated state approaches to the limiting trajectory in the manifold, *i.e.*, to the bluest state for the up-going initial state or the reddest state for the down-going initial state, depending on the direction (up- or down-going) of the initial state.

The above discrepancies between the observed results and the simple model calculations indicate that Harmin's calculation based on the quite simple grid structure is too naive to reproduce the actual coherent time evolution in high slew rate regime. To provide enough interpretation for the experimental result further in detail, more elaborate calculations taking into account the actual Stark energy behavior of the atoms are to be required. Concluding this section, in the present experiment only one prominent peak for the ionization spectrum and the discrete transition of the SFI threshold with slew rate in the wide range of n in the highly excited Rydberg states have been observed. These result are inconsistent with the prediction of the incoherent model calculation, and the discrete transition of the SFI threshold field with slew rate observed in the present experiment is considered to be a manifestation of the "*resonance lanes*" in Harmin's model. Thus it is strongly suggested that the coherent interference effect in the time evolution under the pulsed electric field plays decisive role for the transitional behavior in the highly excited Rydberg states.

6 Conclusion

In conclusion, we have investigated the properties of highly excited Rydberg states to establish the way to detect highly excited states selectively with pulsed field ionization method and to see the possible coherent effect in highly excited Rydberg states with $n > 90$ in the pulsed electric field. The experimental results have been obtained for the Rydberg states with the principal quantum number $n = 98 - 150$ in ^{85}Rb.

For the first time, we observed only one prominent peak in the SFI spectrum and a discrete transition of the SFI threshold field with slew rate. The ionization threshold changed to lower value with increasing slew rate for both the p and s states. The ionization threshold values and the critical slew rates depend on the energy position of the low ℓ states relative to the adjacent manifold on the Stark map. This transitional behavior in the field ionization shows regular dependence on the principal quantum number n, thus indicating that this behavior is quite general and applicable to a wide range of highly excited Rydberg states. From these observations, two important points should be noted:

First, the transitional behavior observed here brings us a new powerful method to selectively field-ionize the low ℓ states from the many close-lying states, thus opening a new way to apply the highly excited Rydberg states to fundamental physics research. One of the example of such applications is to search for dark matter axions with a Rydberg-atom cavity detector [15,16,17,18,19]. In our axion experiment, the SFI system using the pulsed electric field is playing the important role: by selecting the shape of the pulse of the applied electric field properly, the differences in the field ionization values between the adjacent levels can be large enough, for example, the value for the $111s$ state is as three times as that for the $111p$ state. Furthermore, the regular dependence on n in the wide range of $n = 98 - 150$ assures us that the present detector can be applicable to the wide range of axion mass.

Second, the behavior of highly excited Rydberg state under the pulsed electric field described above is inconsistent with the incoherent model calculations and strongly suggests that the coherent interference effect in the time evolution on the grid of anti-crossings under the pulsed electric field plays decisive role for the occurrence of such transitional behavior.

Acknowledgments

The author would like to appreciate help from collaborators, Dr. Izumi Ogawa, Dr. Haruhiko Funahashi, Prof. Katsuji Yamamoto, Dr. Tomohito Haseyama, Kentaro Kominato, Masahiro Shibata, Chikara Ooishi and Tomoya Saida.

The author would like to thank collaborators, Yasuhiro Kishimoto and Satoru Yamada not only for helping to carry out the experiment, but also for providing the calculated data and helping to draw the graphics.

The author also would like to thank Prof. Tsutomu Yabuzaki and Prof. Kenichi Imai for critical reading and comment on the manuscript.

And special thanks should be expressed to my academic adviser, Prof. Seishi Matsuki. His lead and suggestions were essential for this work.

References

[1] T. M. Gallagher, *Rydberg Atoms* (Cambridge University Press, Cambridge, England, 1994) and references cited therein.

[2] See for example, S. Haroche, *Fundamental Systems in Quantum Optics*, Les Houches 1990 LIII, p.767 (North-Holland, Amsterdam, 1992), and references cited therein.

[3] R. G. Hullet, E. S. Hilfer and D. Kleppner, *Phys. Rev. Lett.* **55** (1985) 2137.

[4] D. Meschede, H. Walther and G. Müller, *Phys. Rev. Lett.* **54** (1985) 551.

[5] G. Rempe, H. Walther and N. Klein, *Phys. Rev. Lett.* **58** (1987) 353.

[6] A. Rauschenbeutel *etal.*, *Phys. Rev. Lett.* **83** (1999) 5166.

[7] Recent review includes E. Kolb and M. Turner, *The Early Universe,* Addison-Wesley, New York, 1990; G. Raffelt, *Phys. Rep.* **198** (1990) 1; B. Guiderdoni *et al.* (eds.), *Dark Matter in Cosmology, Clocks and Tests of Fundamental Laws*, Edition Frontieres, Paris, 1995.

[8] M.Minowa (ed.), Proceedings of the 2nd RESCEU International Symposium on *Dark Matter in the Universe and its Direct Detection*, Universal Academy Press, Tokyo, 1996.

[9] See for example, M. S. Turner and J. A. Tyson, *Rev. Mod. Phys.* **71** (1999) S145.

[10] R. D. Peccei and H. R. Quinn, *Phys. Rev. Lett.* **38** (1977) 1791.

[11] Modified from the figure in Ref.[40] for simplicity.

[12] G. Raffelt, in Proceedings of the International Workshop on *Beyond the Desert*, Ringberg Castle, Tegernsee, June 8-14, 1997.

[13] J. Preskill et al., *Phys. Lett.* **120B** (1983) 120; L. Abott and P. Sikivie, *ibid* 133; M. Dine and W. Fischler, ibid 137; M. S. Turner, *Phys. Rev. D* **50** (1986) 889.

[14] P. Sikivie, *Phys. Rev. Lett.* **51** (1983) 1415; *Phys. Rev. D* **32** (1985) 2988; L. Krauss *et al.*, *Phys. Rev. Lett.* **55** (1985) 1797.

[15] S. Matsuki and K. Yamamoto, *Phys. Lett.* B **263** (1991) 523.

[16] I. Ogawa, S. Matsuki and K. Yamamoto, *Phys. Rev.* D **53** (1996) R1740.

[17] K. Yamamoto and S. Matsuki, *Nucl. Phys.* B **72** (1999) 132.

[18] M. Tada, *et al.*, *Nucl. Phys.* B **72** (1999) 164.

[19] A. Kitagawa, K. Yamamoto and S. Matsuki, *LANL preprint archive* hep-ph/9908445.

[20] T. W. Ducas, W. P. Spencer, A. G. Vaidyanathan, W. H. Hamilton and D. Kleppner, *Appl. Phys. Lett.* **35** (1979) 382.

[21] H. Figger, G. Leuchs, R. Straubinger and H. Walther, *Opt. Comm.* **33** (1980) 37.

[22] P. Goy, L. Moi, M. Gross, J. M. Raimond, C. Fabre and S. Haroche, *Phys. Rev.* A **27** (1983) 2065.

[23] D. A. Harmin, *Phys. Rev.* A **56** (1997) 232.

[24] M. L. Zimmerman, M. G. Littman, M. M. Kash, and D. Kleppner, *Phys. Rev.* A **20** (1979) 2251.

[25] T. F. Gallagher, L. M. Humphrey, W. E. Cooke, R. M. Hill, and S. A. Edelstein, *Phys. Rev.* A **16** (1977) 1098.

[26] J-L. Vialle and H. T. Duong, *J. Phys.* B **12** (1979) 1407.

[27] T. H. Jeys, G. W. Foltz, K. A. Smith, E. J. Beiting, F. G. Kellert, F. B. Dunning, and R. F. Stebbings, *Phys. Rev. Lett.* **44** (1980) 390.

[28] G. B. McMillian, T. H. Jeys, K. A. Smith, F. B. Dunning and R. F. Stebbings, *J. Phys.* B **15** (1982) 2131.

[29] T. F. Gallagher and W. E. Cooke, *Phys. Rev.* A **19** (1978) 694.

[30] J. H. M. Neijzen and A. Dönszelmann, *J. Phys.* B **15** (1982) L87.

[31] C. J. Lorenzen and K. Niemax, *Phys. Scr.* **27** (1983) 300.

[32] E. Luc-Koenig and A. Bachelier, *J. Phys.* B **13** (1980) 1743.

[33] J. R. Rubbmark, M. M. Kash, M. G. Littman and D. Kleppner, *Phys. Rev.* A **23** (1981) 3107.

[34] D. Kleppner, M. G. Littman and M. L. Zimmerman, in *Rydberg States of Atoms and Molecules*, eds. R. F. Stebbings and F. B. Dunning (Cambridge University Press, Cambridge, England, 1983).

[35] S. Yamada *et al.*, to be published.

[36] Y. Kishimoto *et al.*, to be published.

[37] R. J. Damburg and V. V. Kolosov, in *Rydberg states of atoms and molecules*, eds. R. F. Stebbings and F. B. Dunning (Cambridge University Press, Cambridge, England, 1983).

[38] D. A. Harmin and P. N. Price, *Phys. Rev.* A **49** (1994) 1933.

[39] S. Yamada *et al.*, to be published.

[40] G. Raffelt, in *The Evolution of the Universe*, eds. G. Börner and S. Gottlöber, Dahlem Workshop Report ES 19.